Chapter 4
Experimental Methodology

Upon completion of the computational optimization process, the resulting leading edge fillet was tested in the large-scale, low speed turbine vane cascade located in the Virginia Tech Experimental and Computational Convection Laboratory. A unique element to this facility is a combustor simulator located immediately upstream of the vane cascade. The purpose of the combustor simulator is to generate more realistic inlet conditions for the turbine vane test section. In this chapter, a description of the wind tunnel, combustor simulator, and turbine vane cascade are given, followed by a discussion of the cascade inlet boundary conditions and the measurement techniques used in experimental verification testing of the leading edge fillet. Finally, estimates of the experimental uncertainties associated with the various measurements are presented.

4.1 Wind Tunnel and Combustor Simulator Design

The wind tunnel that was used in the experimental phase of this research is a large recirculating tunnel that has been adapted to simulate the combustor exit flow and first vane passage of an advanced gas turbine engine. An illustration of the wind tunnel, indicating the key features, is shown in Figure 4.1. The flow in the tunnel is driven by a 50 hp axial fan, controlled by a variable frequency inverter, allowing for precise control of the flow rate through the closed loop. To provide thermal control of the bulk flow temperature during closed loop operation, a main finned-tube heat exchanger using water as the heat transfer fluid is located downstream of the fan. Following the main heat exchanger, the flow passes through a honeycomb flow straightener and a series of screens. Immediately upon passing through the flow straightener and screens, the flow is split into a primary flow and two secondary flow paths. The purpose of this flow split is to enable the modeling of a gas turbine combustor. While the primary flow simulates the main hot gas path, the two secondary flows simulate combustor liner coolant and dilution flow. Following the flow split, the primary flow passes through a perforated plate, a duct heater, and additional flow conditioning elements prior to entering the combustor simulator and vane cascade. The purpose of the perforated plate is to provide the necessary pressure drop to achieve the desired flow split, while that of the duct heater

system is to elevate the primary flow temperature above that of the secondary flow. To further increase the temperature differential, the secondary flows are directed through additional water-cooled, finned-tube heat exchangers to decrease flow temperature prior to injection into the combustor simulator as combustor film coolant and dilution flow. Upon recombination of the primary flow with the cooler secondary flows in the combustor simulator, unique temperature and total pressure profiles are generated at the inlet to the vane cascade, entirely dictated by the fluid dynamics of the simulator. The entire motivation behind the design and construction of the combustor simulator was the accurate reproduction of realistic first vane inlet conditions. Immediately following the combustor simulator, the recombined flows pass through the turbine vane cascade and return to the fan inlet.

The design of the combustor simulator was a major undertaking and is attributed to the efforts of many former students. The details of the simulator design and the results of qualification testing are documented in Barringer, et al. (2002). The goal in designing the combustor simulator was to duplicate the fundamental flow field characteristics present in an aircraft engine combustor, and in so doing, to generate more realistic inlet conditions for the downstream vane cascade. To accomplish this, the simulator shares many of the typical design features of an actual combustor. A typical combustor features four distinct injections of airflow: primary air, intermediate air, dilution air, and cooling air. Primary air is injected through the dome of the combustor, often through a swirler, and provides the necessary air for stable combustion. To drive the reaction to completion, intermediate air is injected through a row of holes downstream of the primary combustion zone. Toward the aft end of the combustor, dilution flow is introduced through another row of holes and serves the purpose of reducing exhaust gas temperature to acceptable levels for the first vane. To maintain the combustor liner at acceptable temperature levels, cooling air is typically injected such that a protective layer of cool air forms on the liner surface. The combustor simulator is similar in design, with two principal exceptions. The first exception is that swirl was not introduced with primary flow injection. The reason for this omission is that in actual combustor design, the swirl introduced by the swirler is often purposefully cancelled by downstream flow injections. The primary purpose of the swirl is to stabilize the combustion process,

however, the presence of swirl at the inlet to the turbine is not deemed advantageous. The second more obvious exception in the simulator design is that no combustion takes place. To simulate the heat release of the combustion process, the primary flow temperature is increased by a duct heater, while the bypass flow temperature is decreased through a water-cooled heat exchanger. The maximum hot to cold flow temperature difference that is achievable by these means is small relative to engine conditions; however, the cascade inlet temperature profiles generated are nondimensionally similar to engine profiles and provide a reasonable differential for film effectiveness measurements in the combustor simulator and on the turbine vane endwall. It is believed that the simulator adequately reproduces the fundamental fluid dynamic behavior present in an actual combustor and generates realistic inlet conditions to the vane cascade.

A cut-away view showing the internal details of the combustor simulator is illustrated in Figure 4.2, while the various flow injections are presented in Figure 4.3. The simulator consists of four film-cooling liner panels for injection of cooling flow, two rows of dilution holes for injection of intermediate and dilution flow, and a backward-facing slot at the combustor-turbine interface for injection of additional coolant. To provide independent control of the various flows, each liner panel and dilution row is fed by a separate flow plenum as shown in Figure 4.2. To meter the flow through the panels and dilution holes, the inlet to each flow plenum was fitted with an adjustable area control. From measurement of the total to static pressure differential, Δp, across each liner panel, the mass flow rate through each panel was calculated using experimentally determined discharge coefficients, according to equation 4.1.

$$\dot{m}_{panel} = C_d \sqrt{2 \rho \Delta p}\, N\, A_{hole} \tag{4.1}$$

The discharge coefficients used in the calculations are summarized in Table 4.1 along with the hole count, N, and hole diameter, D_{hole}, for each liner panel. To determine the flow rates through each row of dilution holes, pitot-static probes were centerline-mounted inside the supply pipes. Since the length to diameter ratio of the dilution supply pipes is low (<3), the flow inside never becomes hydrodynamically fully-developed, thus, the

pitot-static probe measurements provide reasonably accurate estimates of flow rate using equation 4.2.

$$\dot{m}_{dilution} = \sqrt{2\rho\Delta p}\, N\, A_{hole} \tag{4.2}$$

Details of the dilution hole geometries are also presented in Table 4.1 and Figure 4.4.

The backward-facing slot present in the combustor design is a product of the interface between the combustor and high pressure turbine, and is primarily needed to account for mismatch in thermal expansion between the two components. Rather than attempting to eliminate the thermal expansion mismatch, the interface is designed to act as a cooling slot to provide additional thermal protection to the vane endwall. For both the simulator and the combustor after which it was modeled, flow exiting the slot is metered through feed holes and an array of pin. To determine the flow rate exiting the slot, the pressure drop across the feed holes was measured and a discharge coefficient for the holes of 0.70 was assumed. In the experimental phase of this investigation, the slot was initially eliminated from the combustor simulator configuration; however, it was ultimately reintroduced with slight modification to evaluate fillet robustness at altered inlet conditions. The modified slot geometry is presented in section 4.4.

4.2 Wind Tunnel Flow Thermal Conditioning

Given the importance of flow thermal conditioning to this study, it was deemed essential to include further details in a separate section. The key elements of the thermal conditioning system are the primary flow duct heater, the main heat exchanger, and the two secondary flow heat exchangers. To minimize experimental uncertainty in this investigation, it was highly desirable to maximize the thermal driving potential at the inlet of the turbine cascade. This goal was accomplished through the optimized operation of each element of the thermal conditioning system.

The duct heater used to elevate the temperature of the primary flow, shown in Figure 4.5, is a 480 V, 3-phase resistive system and consists of three independently controllable zones. Each heater zone consists of 6 Watlow 375 finned strip heaters wired in a 3-phase Delta configuration, with each side of the Delta consisting of two strip

heaters in parallel, as illustrated in Figure 4.6. Given the nominal resistance of each finned strip heater is 75.5 ohms, the maximum power output of each zone is calculated to be 18.3 kW using equation 4.3,

$$W_{Delta} = \frac{3V_L^2}{R} \tag{4.3}$$

where R is the parallel resistance of each side of the delta. The maximum combined output of the heater system is thus 55 kW. Power to each heater zone is controlled using a PID controller in conjunction with a Watlow DIN-A-MITE solid state power controller. Though the PID controllers are capable of heater exit temperature control, they were operated in proportional control mode for the purposes of this investigation. To maximize the temperature rise of the primary flow, the heaters were operated at 100% output in all experiments. At a nominal primary flow rate of 1.8 kg/s, an air temperature rise of approximately 30°C was measured across the bank of heaters. From an energy balance on the duct heater, the anticipated air temperature rise is calculated to be 30 K, as given in Equation 4.4, showing excellent agreement with observation.

$$\Delta T_{heater} = \frac{q_{heater}}{\dot{m}_{primary} c_p} = \frac{55\,kW}{(1.8\,kg/s)(1.01\,kJ/kg\cdot K)} = 30\,K \tag{4.4}$$

The temperature rise across the duct heater was monitored throughout all experiments as an indicator of heater health. The heater surface temperature at typical operating conditions was in excess of 150°C, as indicated by a surface mounted thermocouple probe. For safety, a maximum temperature limit of 165°C was set for the heater surface using a Watlow limit controller/alarm. If the temperature exceeded the set limit, as would occur if the flow of air were significantly reduced, the limit controller would shut down the duct heater to prevent burn-out.

While the duct heater serves to increase the temperature of the primary flow, heat exchangers in the secondary flow ducts are used to decrease the temperature of the combustor simulator cooling and dilution flow. The heat exchangers are finned-tube, air-

to-liquid units manufactured by Super Radiator Coils. Initially, tap water was utilized as the heat transfer fluid in the heat exchangers, however, the temperature of the tap water was observed to fluctuate throughout the course of a day as well as with the seasons. To eliminate these temperature fluctuations, a recirculating chiller system was installed to provide thermally conditioned water to the main and secondary flow heat exchangers. The chiller is a portable water-cooled unit manufactured by Freeze-Co Systems with a rated heat load capacity of approximately 40 kW (based on a condenser water temperature of 30°C and process supply temperature of 5°C). Additional system heat load capacity, in excess of 40 kW, was realized in this investigation due to lower condenser water temperature (~15°C) and higher process water supply temperature (~10°C). Two fundamental benefits were realized with the addition of the chiller. First, the chiller allows for precise control of the heat exchanger water supply temperature, which was not possible using tap water. The second benefit of the chiller is overall lower water supply temperatures than available with tap water. The measured air temperature drop across the secondary heat exchangers at a nominal air flow rate of 1.1 kg/s was approximately 22°C. From an energy balance on one of the secondary flow heat exchangers, the rate of heat removal can be calculated using equation 4.5.

$$\begin{aligned} q_{\text{secondary hx}} &= \dot{m}_c c_p \Delta T_c \\ &= (1.1\,\text{kg/s})(1.01\,\text{kJ/kg}\cdot\text{K})(22\,\text{K}) \approx 24\,\text{kW} \end{aligned} \tag{4.5}$$

The calculated total heat removal rate for both secondary flow heat exchangers is approximately 48 kW. Under this heat load, the chiller is capable of supplying water at a temperature between 8 and 10°C.

Upon addition of the chiller to the thermal conditioning system, the wind tunnel was run to determine how to best operate the system to achieve the maximum possible thermal driving potential at the inlet to the vane cascade. From these efforts, it was found that minimizing heat removal at the main heat exchanger was desirable. During initial testing, the chiller was used to supply conditioned water to both the secondary flow heat exchangers and the main heat exchanger; however, this configuration resulted in too much heat load on the chiller and consequently a high water supply temperature to the

heat exchangers. To reduce the heat load on the chiller, the main heat exchanger was switched to tap water supply. Upon making the switch, the chiller did not have sufficient heat load and would cycle on and off, causing unacceptable low frequency temperature oscillations in the wind tunnel. To eliminate chiller cycling, the water flow rate through the main heat exchanger was reduced, thereby reducing the rate of heat extraction and temperature drop across the main heat exchanger. By reducing the temperature drop across the main heat exchanger, the inlet air temperature to the secondary flow heat exchangers increases. From a heat transfer perspective, this creates greater driving potential for heat transfer and therefore increases the rate of heat rejection to the secondary flow heat exchangers. The rate of heat rejection to a heat exchanger can be expressed by Equation 4.6,

$$q_{hx} = UA\Delta T_m \tag{4.6}$$

where U is the overall heat transfer coefficient, A is the heat transfer area, and ΔT_m is the mean temperature difference between the air and heat exchanger surface. While U and A remain essentially fixed for given air and water flow rates, ΔT_m increases with inlet air temperature. The UA product for the secondary flow heat exchangers at a nominal air flow velocity of 1.1 m/s and water flow rate of 10 gpm is estimated to be 0.7 W/K.

From a thermodynamic perspective, reducing the rate of heat rejection in the main heat exchanger necessitates increased heat rejection elsewhere. Performing an energy balance on the entire wind tunnel system yields the following expression.

$$q_{heater} - 2q_{secondary\ hx} - q_{main\ hx} - q_{loss} + q_{fan} = 0 \tag{4.7}$$

In equation 4.7, all significant heat addition and rejection terms are represented. q_{loss} represents the heat loss through the walls of the wind tunnel to ambient room conditions, while q_{fan} is the rate of thermal heat addition due to fan and motor inefficiencies. Relative to the other terms in the energy balance, q_{loss} and q_{fan} are small, so for the purposes of this analysis, they are assumed to cancel each other out, having zero net effect. Therefore, for a fixed value of q_{heater}, if $q_{main\ hx}$ decreases, $q_{secondary\ hx}$ must increase

to maintain the energy balance. Since the main heat exchanger conditions the entire flow, it makes no contribution to achieving a temperature differential between the primary and secondary flows. A theoretical maximum achievable temperature difference between the primary and secondary flows can be calculated by assuming $q_{main\ hx}$ is zero. Under this assumption and at steady state, the rate of heat extraction in the secondary flow heat exchangers must equal the rate of heat addition through the duct heater, and the theoretical maximum possible temperature difference can be expressed by Equation 4.8.

$$\Delta T_{max} = T_{exit,heater} - T_{exit,secondary\ hx} = \frac{55\,kW}{\dot{m}_{primary} c_p} + \frac{55\,kW}{\dot{m}_c c_p} \approx 55\,°C \tag{4.8}$$

Unfortunately, the chiller can not support a 55 kW heat load and deliver water at a reasonably low temperature. Additionally, as the temperature of the chiller water supply increases, the flow and surface temperatures throughout the wind tunnel also increase to unacceptable levels. As previously mentioned, a maximum allowable heater surface temperature of 165°C was set for safety, while material limits dictated a maximum operating temperature of 70°C for the vane test section. Ultimately, to maintain the heater and vane temperatures within acceptable limits, some heat removal at the main heat exchanger was required. The necessary heat removal was accomplished using tap water at a nominal flow rate of 2.5 gpm, providing a 1 to 2°C temperature drop across the main heat exchanger. The rate of heat rejection in the main heat exchanger is given in Equation 4.9.

$$q_{main\ hx} = \dot{m}_{total} c_p \Delta T_{main\ hx} = (4.0\,kg)(1.01\,kJ/kg \cdot K)(1.8\,K) \approx 7\,kW \tag{4.9}$$

Operating the system under these conditions yielded a maximum temperature differential between the primary and secondary flows of approximately 52°C, slightly less than the theoretical maximum of 55°C. Upon mixing of the primary and secondary flows in the combustor simulator, the maximum temperature differential at the inlet to the vane cascade was measured to be between 28 and 30°C. Standard operating conditions for the

flow thermal conditioning elements are summarized in Table 4.2, while typical flow temperatures throughout the wind tunnel are presented in Figure 4.7.

4.3 Turbine Vane Cascade Design

The design of the turbine vane test section (Radomsky and Thole, 2000) was guided by the objective to maximize the scale factor while maintaining the ability to establish periodic flow in the vane passages. The principal purpose for maximizing the scale factor was to enable measurements with high spatial resolution. A central vane, two passage cascade was designed on the belief that flow periodicity could be obtained through the use of several flow control devices. These controls include variable bleeds on the outer two partial vanes and a flexible pressure-side outer wall. An illustration of the vane cascade and combustor simulator, indicating the key features of both, is shown in Figure 4.8. Using the flow controls, the midspan pressure distribution on the central vane was matched to that determined computationally from a two-dimensional inviscid CFD simulation with periodic boundary conditions. The variable bleeds allow for proper adjustment of the stagnation locations on the outer two vanes, while the flexible wall permits fine tuning of the flow acceleration in the outer passage. The vane pressure distribution is expressed nondimensionally by the pressure coefficient or Euler number as defined in equation 4.10. A comparison of typical experimental pressure coefficient distributions with the results of CFD is presented in Figure 4.9.

$$C_p = \frac{p_s - p_{s,inlet}}{\frac{1}{2}\rho U_{inlet}^2} \tag{4.10}$$

Flow periodicity is demonstrated in Figure 4.10 for both low and high freestream turbulence conditions (Radomsky, 2000).

To enable visual access, the predominant material of construction for the cascade test section is acrylic, with exception to the airfoils and measurement endwall, which are constructed of polystyrene foam overlaid with fiberglass and polyurethane foam, respectively. A photograph of the cascade is presented in Figure 4.11. The side walls of the cascade, including the flexible side wall, are constructed of acrylic, allowing for

optical measurement techniques to be employed. The non-measurement endwall, or cascade lid, was constructed of several different materials to satisfy different measurement needs. For infrared camera measurements, an acrylic lid with numerous circular viewing ports was used. When a viewing port was not being used for thermal imaging, an acrylic blank was inserted to seal the cascade.

The measurement endwall of the cascade was constructed of a low thermal conductivity ($k_{endwall}$ = 0.037 W/m K), closed cell polyurethane foam sheet (1.3 cm thick) backed by a ¾ inch sheet of plywood for structural strength. The polyurethane foam is produced by General Plastics Manufacturing Company, and is primarily used in the construction of aircraft interior panels and overhead luggage compartments. The turbine vanes were constructed of extruded polystyrene foam insulation (k_{vane} = 0.029 W/m K) overlaid with fiberglass cloth to achieve a smooth flow surface. The polystyrene foam is a product of Pactiv Corporation (formerly Tenneco Packaging Inc.), and is used as an exterior insulation and sheathing in residential and commercial construction. To construct the vanes, the vane profiles were cut multiple times from a 2 inch thick polystyrene sheet, and the foam pieces were stacked and bonded together to achieve the full span height. During the assembly, pressure taps were inserted near the vane midspan to enable measurement of the vane pressure distribution. The taps were constructed from 0.0625 inch outer diameter copper tubing and were positioned normal to the vane surface during assembly. After assembly, the foam was overlaid with fiberglass cloth and an epoxy resin-hardener mixture to create a smooth flow surface. The static pressure taps were slightly chamfered to eliminate any burs that might affect the pressure readings. The principal reason for the use of foam in the construction of the turbine vanes and measurement endwall was their associated low thermal conductivity. Low thermal conductivity enables these flow surfaces to be modeled as adiabatic, and allows for the direct measurement of film cooling effectiveness.

4.4 Cascade Modifications to Accommodate Fillet Testing

To match the thermal conductivity of the measurement endwall, the fillet ultimately tested was also constructed of polyurethane foam. The geometry was sent to General Plastics and two fillets were machined from solid blocks of the foam. To enable

the fillets to wrap around the existing vane, the vane profile was first removed from the foam block, followed by the machining of the fillet surface shape. The tested fillet has a linear profile shape, with a maximum height and extent of 9.5 cm. The locations of maximum height and extent are both along the suction surface of the vane near the geometric stagnation point. In the installation of the fillets, one was placed about the center vane while the other was split at the leading and trailing edges to accommodate the outer two partial vanes. Special foam pieces were constructed to transition the outer fillet geometries into the variable bleeds. Figure 4.12 is a photograph of the completed installation.

To accommodate fillet testing, modification of the combustor simulator was necessary. The original combustor simulator configuration included a backward-facing coolant slot directly upstream of the vane leading edge; however, due to interference issues with the linear leading edge fillet tested, the slot was eliminated from the combustor design. This slotless configuration is illustrated in Figure 4.13. Upon completion of fillet testing with the slotless design, it was decided to reintroduce the slot, placing it further upstream of the vane leading edge to avoid any interference issues with the fillet. To reintroduce the slot, a transition piece between the combustor simulator and vane cascade was manufactured whereby the distance between the two was increased. Effectively, this new transition increased the amount of flat endwall upstream of the vane leading edge to accommodate the addition of the slot geometry. The modified interface geometry is illustrated in Figure 4.14. Due to geometric constraints, the slot feed hole orientation also had to be modified as shown, however the number, diameter and spacing of the feed holes were held fixed, as given in Table 4.1. With the modified slot configuration, the fillet was tested at two different slot mass flow rates achieved by varying the number of feed holes. To achieve the design slot mass flow rate, 13 feed holes were spaced 7.6 hole diameters on center. To approximately double the slot flow rate, 14 additional feed holes were added, halving the feed hole spacing to 3.8 hole diameters on center. Photographs of the slot installation are presented in Figure 4.15.

4.5 Vane Cascade Inlet Boundary Conditions and Test Matrix

Four inlet boundary conditions and two combustor/cascade interface configurations were considered in this investigation to determine fillet effectiveness and robustness in reducing endwall adiabatic temperature levels relative to a baseline, unfilleted vane. Two of the tested inlet conditions were for a flush endwall interface, while the remaining two featured a backward-facing slot at the interface. For each inlet condition, baseline tests without a fillet and tests with the fillet were conducted.

For the flush endwall interface, thermal performance of the fillet was examined for two different inlet total pressure profiles: the design profile and an off-design profile. Both inlet profiles feature a near-wall peak in total pressure, which is characteristic of the flow exiting a typical combustor. The nominal design peak was roughly doubled to evaluate robustness of fillet performance to a change in total pressure profile. As presented in Chapter 3, the measured inlet total pressure profiles are shown in Figure 4.16 in comparison to those applied in the computations. Named according to the nominal value of the nondimensional total pressure peak, the design and off-design profiles are also referred to as $\Delta p_{o,max} \approx 1$ and $\Delta p_{o,max} \approx 2$, respectively. To create the profiles, the amount of flow exiting each of the combustor liner panels was adjusted, according to Table 4.3. Specifically, to generate the off-design profile, the mass flow exiting the last two liner panels (Panels 3 and 4) was significantly increased while panels 1 and 2 were completely closed. Since the flow and thermal fields exiting the combustor simulator are interdependent, altering the inlet total pressure profile also results in a change to the inlet thermal field. Figure 4.17 presents pitchwise averaged inlet profiles of nondimensional temperature for both inlet total pressure conditions. Interestingly, the maximum flow temperatures measured in the near-wall region for the off-design condition are higher than those measured for the design condition, despite increased coolant flow exiting panels 3 and 4. This is attributed to the higher momentum flux ratios of the coolant jets, which results in enhanced mixing between the coolant and mainstream. In addition to enhanced mixing, the coolant film generated by panels 1 and 2 for the design inlet condition is not present for the off-design condition. Thus, the coolant exiting panels 3 and 4 at off-design conditions is injected into a higher temperature environment. Turbulence levels at the inlet to the cascade were measured by Barringer et al. (2002) to

be between 15 and 18%, while the integral length scale was calculated to be on the order of the dilution hole diameter.

For testing with the backward-facing slot, the inlet total pressure profile above the slot was held fixed at the design condition while the mass flow rate of coolant exiting the slot was varied. Two slot flow rates were studied: the design flow rate and approximately twice the design flow rate. The flow rate of coolant was roughly doubled from the design value by increasing the number of slot feed holes from 13 to 27. Percentage slot flow for the design and off-design conditions are 0.42% and 0.84% of the total cascade flow rate, respectively, as indicated in Table 4.3. A summary of all tested configurations is provided by the experimental test matrix, presented in Table 4.4.

4.6 Pressure Measurements

Several different pressure sensing devices were used in this investigation. Static pressure taps were used to sense the pressure differential across each of the combustor panels and slot feed holes. As previously mentioned, static taps were also placed about the vane midspan to enable measurement of the pressure distribution. To measure the total pressure profile at the inlet to the vane cascade, a rake consisting of four Kiel probes was used. The Kiel probes were evenly-spaced 1.27 cm apart, as shown in Figure 4.18. A distinguishing feature of the Kiel probe is its shrouded flow impact port. The purpose of the shroud is to decrease probe alignment sensitivity by forcing the local flow to align with the shroud axis and directly impact the measurement port. This feature of the Kiel probe makes it ideally suited for measurement of total pressure in fluid flows where the flow direction is unknown or varies with operating conditions. The Kiel probes used in this investigation were manufactured by United Sensor Corporation, and are insensitive to yaw angles up to 52° and pitch angles up to 40°.

To measure these sensed pressures and pressure differentials, several pressure transducers of varying input range were used. To maximize measurement precision, pressure transducers were matched to the sensed pressure, choosing a transducer with the smallest suitable range for a given measurement. The transducers utilized in this investigation were sourced from two companies: Omega Engineering and Setra, and their characteristics are tabulated in Table 4.5. All transducers are high accuracy, low pressure

differential, variable capacitance transducers. To communicate the sensed pressures to the transducers, flexible urethane or vinyl tubing was used.

4.7 Velocity Field Measurements

Two methods of measuring flow velocity were used in this investigation. The first of these methods was the use of conventional pitot-static pressure probes, while the second was Laser Doppler Velocimetry (LDV). As previously mentioned in section 4.1, pitot-static probes were centerline mounted in the dilution feed pipes to enable setting of the dilution flows. In addition, a pitot-static probe was used to take point measurements of velocity at various locations throughout the vane cascade, providing a quick check of the anticipated flow velocity. However, the pitot-static probe was not used to generate velocity profiles due to its directional sensitivity. Unlike the Kiel probes used to measure the cascade inlet total pressure profile, the pitot-static probe is highly sensitive to orientation in the flow.

To perform detailed flowfield measurements, a two-component fiberoptic LDV system manufactured by TSI Incorporated was used. The key components of the LDV system are a model 9201 Colorburst multicolor beam separator, a model 9230 ColorLink multicolor receiver, an IFA 755 digital burst correlator, and a model 9832 two-component fiberoptic probe. The source of coherent light for the system is a 5W Spectra-Physics Stabilite 2017 Argon Ion laser. The laser provides maximum power output at the Argon lines used for velocity measurement, which are 514.5 nm (green) and 488.0 nm (blue). The Colorburst multicolor beam separator separates the measurement wavelengths from the other Argon lines, and splits the measurement beams into shifted and unshifted beam pairs, with the shifted beams passing through Bragg cells. Beam shifting enables determination of flow direction as well as velocity magnitude, making the LDV uniquely suited to performing measurements in regions of flow reversal. The measurement beams are then launched into the fibers of the probe using specially designed fiberoptic couplers, that facilitate optimum coupling of the light for maximum fiber throughput. The fiberoptic probe not only transmits the two measurement beam pairs, but also collects backscattered light from seed particles as they pass through the measurement volume. The backscattered light is transmitted through a receiving fiber to

the ColorLink multicolor receiver, where it is amplified and converted into electrical signals by two photomultiplier tubes, one for each measurement wavelength. Finally, the electrical signals are analysed by the IFA 755 digital burst correlator and the two components of flow velocity are calculated. Several different probe focusing lenses are available to enable measurement at various penetration depths into the cascade. The standard focusing lens utilized with the probe has a 350 mm focal distance. To extend the focal distance, a 2.6X beam expander can be used with either a 450 mm and 750 mm focusing lenses. The purpose of using a beam expander at these extended focal lengths is to maintain a relatively small measurement volume. To control the system hardware and collect velocity data, TSI's FIND (Flow Information Display) software was utilized.

In this investigation, flow velocity measurements were performed in the vane stagnation plane for the original combustor simulator configuration. To enable measurements in the stagnation plane of the center vane, the probe beam expander was used in conjunction with the 750 mm focusing lens. This system configuration gave a measurement volume length and diameter of 0.85 mm and 73 microns, respectively. To seed the flow, a specially-designed olive oil atomizer was used (Radomsky, 2000). Both streamwise(U) and spanwise(W) components of velocity were measured with a typical sample size of approximately 10,000 data points. At a typical data rate between 200 and 300 points per second, sampling time ranged from approximately 30 seconds to 1 minute. Residence time weighting was applied in data processing to correct for residence time bias errors. Measurement results are presented in Chapter 6.

4.8 Temperature Measurements

Two means of temperature measurement were used in this investigation. For direct contact measurements of temperature, conventional thermocouples were utilized, while non-contact, non-invasive measurements were performed using an infrared camera. This section presents the details of temperature measurement using conventional thermocouples, while the infrared camera measurement procedures are discussed in section 4.10.

For all direct contact measurements of temperature in this investigation, Type E (Chromel-Constantan) thermocouples were used. The principle reason for selection of

type E thermocouples is their associated high Seebeck coefficient. Higher than any other standard thermocouple, the Seebeck coefficient for type E is 62 μV/°C at 20°C. To ensure uniformity of the metal alloys, all thermocouple wire and connectors used in this study were obtained from Omega Engineering. Additionally, all thermocouple junctions were created using a Tungsten Inert Gas (TIG) welding system manufactured by Tigtech, Inc. of Lexington, Massachusetts. The Tigtech Model 116 SRL welder employs an electric arc in an argon atmosphere to generate the necessary heat to melt the thermocouple wires and form a junction. The argon gas prevents oxidation of the molten metal, yielding strong and consistent thermocouple junctions. 30 AWG wire was used in the manufacture of nearly all thermocouple elements, resulting in a typical bead diameter of approximately 1 mm. A typical welded thermocouple junction is shown in Figure 4.19.

Measurements of temperature in this investigation included various mean flow temperatures throughout the wind tunnel, endwall, fillet, and vane surface temperatures, and detailed thermal field measurements in select flow planes. To ensure steady state conditions had been achieved, mean flow temperature at the inlets to the main heat exchanger, the heater bank, and the combustor simulator were continually monitored during all experiments. Additionally, the mean flow temperatures in each combustor coolant supply chamber were also monitored. These measurements not only provided verification of steady state conditions, but also provided useful information regarding the performance of each component of the thermal conditioning system. For example, loss of power to a portion of the duct heater bank could be quickly detected by a drop in combustor inlet temperature, and the rate of heat rejection through each heat exchanger could be determined from the measured temperature differential. To ensure good measurements of flow temperature, the sensing thermocouples were typically extended out into the flow through metallic tubing for support, with the thermocouple beads directly exposed. In addition to the mean flow measurements, thermocouples were embedded in the vane passage endwall surface for purposes of infrared camera calibration. For testing with a leading edge fillet, additional thermocouples were embedded in the fillet surface. All surface-mounted thermocouples were carefully

threaded through the endwall and fillet surfaces, allowing the thermocouple beads to lay flush.

To measure the thermal field in the vane cascade, two thermocouple rakes were specially designed and fabricated. Specifically, the rakes were designed to measure the thermal field in the SS2 plane, as shown in Figure 3.21. The SS2 plane was selected for measurement based on computational results, which showed that the thermal field in this plane is a good indicator of fillet performance. The reason that two separate thermocouple rakes were required is due to the change in endwall shape with the addition of the fillet. For thermal field measurements without the fillet, a rake with a linear array of thermocouple elements was constructed, while for measurements with the fillet, a rake with a profiled array of thermocouples was necessary. The primary objectives in rake design were to maximize the spatial resolution of the measurements and to minimize rake drag and flow disturbance.

In designing the thermocouple rakes, it was considered imperative to be able to completely map the SS2 plane with a single traverse of the rake. Due to the location and orientation of the traverse system, designing a rake requiring multiple traverses would require intermediate repositioning of the probe or relocation of the existing traverse system, both of which are problematic. Relocating the probe between traverses could potentially introduce positioning errors, while relocation of the existing traverse system would necessitate the design of a new cascade lid to allow probe access. For these reasons, achieving a complete mapping of the SS2 plane in a single traverse was set as a design constraint. The vane to vane distance in the SS2 plane dictated the width of the rake to be 4.25 inches (108 mm). This width allowed for reasonable clearance between the rake and vane surfaces as the rake was traversed from the endwall position to midspan.

The basic concept behind the design of the rakes was to have multiple thermocouple elements or fingers extending from a common boom, with each element consisting of a thermocouple passing through a small diameter metallic tube for rigidity and precise placement. To minimize rake drag, it was advantageous to contain the thermocouple wires internal to the rake. To achieve this, the boom was constructed from hollow aluminum tubing having an aerodynamic airfoil-like cross-section. In addition,

the thermocouple wires were channeled from the boom through a larger diameter tube, which also served as a means of connecting the rake to the traverse system. In determining the number of thermocouples and the thermocouple finger diameter, consideration was given to the amount of flow blockage that would result. To minimize flow disturbance and rake drag, it was deemed beneficial to minimize the amount of blockage introduced by the rake. Figure 4.20 presents a simple conservation of mass argument illustrating the effect of rake blockage ratio on the flow field. Minimum flow blockage is accomplished by maximizing the element pitch to diameter ratio; however, element pitch is primarily dictated by the desired measurement spatial resolution. Therefore, the objective becomes to minimize thermocouple element diameter. Ultimately, a thermocouple spacing of 0.25 inches(6.4 mm) and a finger diameter of 0.0625 inches(1.6 mm) were selected, yielding a 17 element rake with a blockage ratio of 25%. The resulting two rakes are shown in Figures 4.22 and 4.23.

The thermocouple wire used in the manufacturing of the rakes was 30 AWG Type E with Teflon insulation. To minimize response time, the rake elements were designed to have exposed junctions. To pass the thermocouple wire through the small inner diameter of the brass tubing, the outer layer of Teflon insulation had to be removed taking caution not to damage the insulation on the individual wires. Threading of the wire through the tubing had to be done prior to welding the thermocouple junction, as the resulting junction diameter is slightly larger than the inner diameter of the tubing. Typical junction diameter is 0.035 ± 0.002 inches(0.89 ± 0.05 mm), while the brass tubing inner diameter is approximately 0.032 inches(0.8 mm), as shown in Figure 4.21. To minimize thermocouple impedance, the length of thermocouple-grade wire was limited to a maximum of approximately 6 feet(1.8 m). The thermocouple-grade wire was then terminated with like-type miniature male connectors, which could be plugged into one of two jack panels for connection to the data acquisition system. After all the thermocouple elements were manufactured and the rake boom machined, all pieces of the rake were carefully brought together and held in a fixture to ensure precise positioning. To permanently secure the elements of the rake, a quick setting epoxy was injected into the hollow boom of the rake.

To qualify the two thermocouple rakes, several tests were conducted. First, the rakes were subjected to near isothermal conditions to determine if any unacceptable measurement bias existed between the elements. This comparison was done at both low and elevated temperatures, and all thermocouples were observed to agree within 0.1°C. The second test involved comparison of a measured temperature profile between a single element rake and the multi-element rakes. The purpose of this test was to determine if the flow blockage introduced by the multi-element rake affected the measured profile. The results of this test are presented in Figure 4.23, with no blockage effect indicated.

Finally, temperature measurement errors due to thermal interactions between the measurement device and measurement environment, also known as insertion errors, were estimated through analysis. The primary sources of insertion error correspond to the three modes of heat transfer: conduction, radiation, and convection. Conduction error is introduced by the flow of energy to or from the sensing element through the probe structure. For a typical thermocouple probe, conduction through the wire leads and supporting metallic sheath introduce error. Radiation exchange between the temperature sensor and measurement environment can also introduce significant error, especially in high temperature environments. Convection error, also referred to as recovery error, is associated with temperature measurement in high-speed gas flows, where significant conversion of kinetic energy to sensible energy can occur. While the last source of error is irrelevant to this investigation due to the low flow velocities, an estimate of temperature measurement error due to conduction and radiation was calculated through a combined thermodynamic and heat transfer analysis of the thermocouple junction.

Under steady state conditions, an energy balance on the thermocouple bead dictates that the rates of heat transfer attributed to the various modes must equal zero, as expressed by Equation 4.11 and illustrated in Figure 4.24.

$$q_{conv} + q_{cond,A} + q_{cond,B} + q_{rad} = 0 \tag{4.11}$$

Substituting in the appropriate expressions for the various heat transfer modes yields the following.

$$hA_s(T_\infty - T_{TC}) + k_A A_c \frac{dT}{dx} + k_B A_c \frac{dT}{dx} + \varepsilon\sigma A_s(T_{sur}^4 - T_{TC}^4) = 0 \qquad (4.12)$$

Ideally, the junction or bead temperature, T_{TC}, should be equivalent to the local flow temperature, T_∞, therefore, the difference between the two is the error. Rearranging equation 4.12, the error due to conduction and radiation is given by equation 4.13.

$$e_{cond+rad} = (T_{TC} - T_\infty) = \frac{k_A A_c}{hA_s}\frac{dT}{dx} + \frac{k_B A_c}{hA_s}\frac{dT}{dx} + \frac{\varepsilon\sigma}{h}(T_{sur}^4 - T_{TC}^4) \qquad (4.13)$$

Equation 4.13 provides insight into how to minimize the error. Starting with the conduction error term, it is advantageous to use low thermal conductivity wire. Relative to other standard calibrations, type E thermocouple wire has low thermal conductivity, at 17 W/m·K for the nickel-chromium lead and 22 W/m·K for the copper-nickel(Constantan) lead. Additionally, it is advantageous to maximize the thermocouple bead to wire diameter ratio, however doing so increases the response time of the measurement device. A typical bead to wire diameter ratio for the thermocouples used in this investigation is 3.5. To minimize the error due to radiation, the emissivity of the measurement device should be minimized. This was accomplished by welding the thermocouple junctions in an Argon atmosphere, which prevented oxidation of the bead. The emissivity of a typical thermocouple bead is estimated to be 0.2. Finally, both conduction and radiation errors are reduced as the convective heat transfer coefficient, h, increases. Unfortunately, in most measurement situations the heat transfer coefficient is not an independent variable that can be freely varied; rather, it is a function of the measurement environment.

In this analysis, the heat transfer coefficient was calculated using a correlation for forced convection on a sphere proposed by Whitaker (1972). In the freestream, away from wall boundaries, the flow velocity is approximately 6 m/s at the inlet to the vane cascade and estimated at 20 m/s in the SS2 measurement plane. The calculated heat transfer coefficients for these freestream flow conditions are 330 W/m^2·K at 6 m/s and 560 W/m^2·K at 20 m/s. When positioned close to a wall in the boundary layer, the heat

transfer coefficient decreases due to the lower flow velocities and measurement error increases. At 0.9 m/s, the heat transfer coefficient is 150 W/ m^2·K. Based on the measured gradients in flow temperature, the maximum temperature gradient (dT/dx) for conduction in the thermocouple lead wires was estimated to be 1°C/cm, as shown in Figure 4.24. In evaluating the error due to radiation, the thermocouple junction temperature was assumed to be 300 K, while that of the surroundings was taken to be 325 K. Applying these assumptions, the maximum estimated error due to conduction and radiation in the near-wall region is calculated to be approximately 0.75°C, two thirds of which is attributed to conduction. Both conduction and radiation lead to higher thermocouple readings for the typical measurement situation of this investigation. Away from flow boundaries, the estimated maximum error drops quickly to approximately 0.35°C at the cascade inlet and less than 0.25°C in the SS2 plane. Numerical modeling could possibly be used to better evaluate radiation and conduction errors, and could also aid in measurement correction if deemed necessary.

4.9 Adiabatic Effectiveness Measurements

High spatially-resolved measurements of endwall adiabatic temperature were performed with an infrared camera. The use of an infrared camera enabled complete thermal mapping of the vane endwall at a resolution unrealistically achievable using conventional measurement techniques. For example, to realize similar spatial resolution with conventional thermocouple instrumentation would require on the order of 10,000 thermocouples. However, when utilizing infrared measurement techniques, an independent temperature measurement device must be used for calibration purposes, unless knowledge of the measurement surface emissivity and background temperature are available.

The infrared camera utilized in this investigation is an Inframetrics Model 760, shown in Figure 4.25. The Model 760 is a longwave thermal imaging system, detecting thermal radiation in the 8 to 12 μm wavelength range, and features a single Mercury Cadmium Tellurium (HgCdTe) detector cooled to 77 K by an internal microcooler. The microcooler eliminates the need for liquid nitrogen to cool the detector, typical of earlier infrared imaging systems. To produce a thermal image, the Model 760 has a dual

resonant galvanometer scanning system, whereby two internal oscillating mirrors are used to scan the imaged surface. The resulting image consists of 206 x 255 pixels for a total of 52,530 temperature readings. At a nominal focal distance of 55 cm, the image area is approximately 19.4 cm wide by 15.7 cm tall, resulting in a pixel to pixel spatial resolution of less than 1 mm. A separate camera control unit facilitates the imaging process with a 4 inch LCD display and a 1.4 MB floppy drive for storing images to disk. After storage to disk, the images were transferred to a computer for image processing using TherMonitor Lite software, produced by ThermoTeknix Systems Ltd.

The Inframetrics Model 760 infrared camera does not directly measure temperature, rather it detects thermal radiation emitted by a surface and converts the sensed radiation into a temperature based on user-specified parameters. These user-specified parameters are background temperature, T_{bkgnd}, and emissivity, ε, and are used to calibrate the camera in a particular measurement situation. The background temperature represents the average temperature of the environment surrounding the imaged surface, and accounts for background radiation reflected from the imaged surface and intercepted by the camera. The emissivity is a measure of how efficiently the imaged surface emits thermal radiation compared to an ideal emitter. Often referred to as a blackbody, an ideal emitter has an emissivity of 1.0 by definition. The emissivity of a real surface is dependent upon many factors, but as a general rule, highly polished or reflective surfaces have low emissivity, in the range of 0.05 to 0.2, while surfaces characterized by roughness and reentrant cavities have higher emissivity, ranging from 0.8 to 0.99. Due to excessive reflection of background radiation, infrared temperature measurement of highly polished surfaces is difficult and subject to considerable error. The emission of thermal radiation from a polished surface is often a small fraction of the reflected radiation, yielding a situation analogous to having a low signal-to-noise ratio. Fortunately, this problem can be easily rectified in most measurement situations through application of flat black paint to the surface. To achieve the highest possible value of emissivity, the polyurethane foam measurement surface in this investigation was likewise painted black.

To facilitate calibration of the infrared camera, thermocouples were embedded in the measurement endwall, flush with the surface. The typical calibration procedure

involves iterative adjustment of the background temperature and surface emissivity until agreement is achieved between the camera and the thermocouples. In this investigation, a post-measurement approach to infrared camera calibration was employed. The reason for selection of this approach is that it relieves the experimenter from setting and checking the camera calibration throughout the data collection process. In addition, the camera calibration parameters are software selectable during image processing, allowing for post-measurement adjustments to be made. To enable post-measurement calibration, the endwall-mounted thermocouples were continually monitored while infrared images were taken. Using the thermocouple data in conjunction with the image processing software, iterative adjustments were made to the calibration parameters until best agreement was achieved between the thermocouple readings and the image results. This process was repeated for each set of images, and the resulting values of emissivity and background temperature were recorded. While the best fit emissivity was relatively stable from one image location to another, significant variations in background temperature occurred. Initially, the best fit background temperature at each imaging location was used in data extraction, however, this was found to cause significant mismatch of isotherms between adjacent images. Ultimately, an average background temperature was found to work better, resulting in a maximum bias error between the infrared measurement and thermocouple measurement of 1°C.

To get a complete thermal mapping of the vane passage endwall, infrared images were taken at 14 different imaging locations, as illustrated in Figure 4.26, and the collected images were assembled into one composite image of the endwall. As was mentioned in section 4.3, a specially-designed cascade lid with multiple imaging ports was utilized for infrared measurement. To allow direct imaging of the endwall, special port covers where manufactured with thru holes of the same diameter as the infrared camera lens, minimizing flow leakage and associated flow disturbance. When an imaging port was not being used for measurement, a port cover was inserted to seal the cascade. To get a good average at each imaging location, as determined by Kang et al. (1998), five images were taken and frame averaging was employed, whereby each recorded image is the average of 16 frames. During image processing, the five images were subsequently averaged, resulting in temperatures at each pixel location that

represent the average of 80 readings. The maximum precision uncertainty for these measurements was less than 0.2°C.

Prior to assembling the 14 different images into a composite image of the endwall, each image had to be mapped into the global coordinate system. Since the images themselves only contain temperature information at each pixel location, this process entailed assignment of X and Y global coordinates to each pixel in an image. To be able to properly assign global coordinate values, the coordinates of two points in each image must be known, assuming the camera is perpendicular to the imaged surface and the surface is flat. From two known points, the scale and orientation of the image relative to the global coordinate system can be determined as illustrated in Figure 4.27. To facilitate this process, special markers were placed on the cascade endwall at known coordinate locations, ensuring that at least two markers would be visible in each image. Additionally, care was taken to place the markers reasonably far apart in each image to minimize error in the calculated image rotation angle. To perform the coordinate mapping, an existing Fortran program, written by Atul Kohli (1997), was modified and is included in Appendix D. The required inputs to the program are the image temperature matrix and a structured text file containing the pixel coordinates and corresponding global coordinates of two endwall markers. The output of the program is a three column matrix, with the columns corresponding to the global coordinates, X and Y, and the adiabatic wall temperature, T_{aw}. After processing all the files at each imaging location, the individual outputs of the coordinate mapping program are assembled, and regions of overlap between adjacent images are averaged by a final program, also included in Appendix D. Upon completion of this final averaging process, the data are ready for plotting.

Imaging non-planar surfaces, such as the fillet investigated in this study, introduces an additional complication of perspective distortion, whereby two known points in an image no longer suffice in the determination of proper coordinate mapping. Figure 4.28 illustrates this distortion phenomenon using an evenly-spaced grid of points on a flat surface. With the camera positioned perpendicular to the grid surface, the resulting image is free of distortion, as was the case when imaging the flat endwall of the cascade, however, when the surface is inclined, perspective distortion occurs. The reason

for this distortion is that the imaged surface is no longer parallel to the camera "film" plane. The manifestation of perspective distortion is that two points positioned closer to the camera appear farther apart in the resulting image than equivalently-spaced points positioned further away from the camera. Similarly, the inclination and curvature of the fillet resulted in perspective distortion during infrared imaging.

To correct for the perspective distortion introduced by the fillet, calibration images were taken of a specially-crafted reference template wrapped onto the fillet surface. The template, shown in Figure 4.29, was constructed from stainless steel foil and consists of a grid of known reference points. The grid was created by painting the foil black followed by carefully scratching the paint away in the desired pattern. Prior to taking calibration images, measures had to be taken to ensure that each time images were taken, the infrared camera would be positioned in precisely the same way. This was accomplished by using small brass alignment pins to fix camera positioning at each image location. Additionally, an acrylic mounting fixture was designed and built for the camera. Alignment holes in the base of the acrylic fixture and in the various port covers would accept the brass pins and correctly align the camera every time. Figure 4.30 presents a photograph that demonstrates camera alignment. To quantify the error associated with this alignment method, several calibration images were taken at the same location, in between which the camera was completely refixtured. The maximum observed change in pixel location of a template reference point was less than three pixels, which is equivalent to roughly 2.5 mm. A typical fillet calibration image is presented in Figure 4.31.

After completing all the calibration images, the pixel coordinates of each reference point in every image were determined using the TherMonitor Lite software. Next, these pixel coordinates were matched to their corresponding endwall global coordinates, X and Y. Using these coordinate pairs as input, a new image processing program was written in Matlab to perform global coordinate mapping. A linear interpolation function based on a Delaunay triangulation of the data was used to assign global coordinates to all pixels in between the known reference points. The interpolation function used does not extrapolate to points that fall outside of the reference set. Thus, pixels located outside the convex hull of the reference point data set were not assigned

global coordinate values. Similar to the Fortran image processing program, the output of this program is a three column matrix, with the columns corresponding to the global coordinates, X and Y, and the adiabatic wall temperature, T_{aw}. The Matlab program is included in Appendix E.

4.10 Data Acquisition System

The data acquisition system utilized in this investigation consists of a National Instruments AT-MIO-16E-2 analog-to-digital (A/D) board and a National Instruments SCXI (Signal Conditioning eXtensions for Instrumentation) front-end. Programming and control of the data acquisition system was performed using LabVIEW software, also a product of National Instruments.

The A/D board is a multifunction I/O (input/output) board specifically designed for use with an AT series personal computer. The board has 16 single-ended/8 differential inputs, each independently programmable for polarity and range. The gain for each channel is also independently selectable as the board features a programmable gain instrumentation amplifier (PGIA). This allows for matching of the input signal ranges to those that the ADC (analog-to-digital converter) can accommodate, ensuring the highest possible measurement precision. The ADC has a bipolar input range of -5 to 5 V and 12 bit resolution. The maximum aggregate sampling rate achievable is 500 kS/s, limited by the 2μs settling time of the circuitry.

The signals digitized by the A/D board are first conditioned using a National Instruments SCXI signal conditioning system. The SCXI family of products has a modular system architecture, whereby a system chassis is capable of accepting a variety of different modules designed for various signal conditioning needs. To accommodate the measurement requirements of this investigation, an SCXI 1000 chassis with three SCXI 1100 signal conditioning modules were used. The SCXI 1100 module is a 32-channel multiplexer and amplifier. The 1100 module multiplexes the 32 differential input channels into a single software-programmable gain instrumentation amplifier. The output of the amplifier is then passed to the chassis bus and through a shielded cable to the A/D board to be digitized. Two of the three SCXI 1100 modules were used to condition thermocouple signals, while the third module was dedicated to the higher

voltage output of the pressure transducers utilized in this study. Connection of the thermocouple signals to the signal conditioning system was accomplished using an SCXI-1303 terminal block. The SCXI-1303 terminal block was specifically designed for high-accuracy thermocouple measurements, featuring isothermal construction to minimize error due to thermal gradients between terminals and an integral cold junction reference sensor. The cold junction sensor employed in the terminal block is a thermistor (thermally sensitive resistor) with a nominal sensitivity of -24.2 mV/°C and an accuracy of ±0.65°C at 25°C. The output voltages of the pressure transducers were connected through an SCXI-1300 general-purpose terminal block.

To facilitate easy connection of thermocouple signals to the data acquisition system, two custom junction boxes were manufactured. Each box was built around a standard Omega Engineering jack panel, one having 36 female connectors and the other 24 female connectors. The junction boxes were designed to be somewhat mobile, each featuring an umbilical of extension-grade thermocouple wire terminating with a SCXI-1303 terminal block. This design flexibility allowed the 24 channel junction box to be mounted onto the traverse system for use with thermocouple rakes. An additional benefit of the junction boxes was the ability to customize the channel arrangement of thermocouple connections.

The LabVIEW programs or virtual instruments used for data collection were modified versions of programs written by National Instruments for use with their data acquisition hardware. For taking pressure measurements, a standard voltage measurement program was modified to include the pressure transducer calibration characteristics, enabling the measured voltage signal to be converted and displayed in units of pressure. To minimize the quantization error associated with the pressure measurements, a gain of 2 was applied to the transducer output voltages, matching the output range of the transducers to the input range of the A/D board. For temperature measurement and recording, a standard temperature measurement virtual instrument was modified to enable multiplexing across multiple SCXI 1100 modules. The original program limited temperature measurement to a maximum of 32 channels on 1 module; however, more measurement channels were needed. The modified multi-module temperature measurement program satisfied this need. The amplifier gain applied in the

temperature measurement was selected by the program based on the user specified temperature range.

In this investigation, all tests were conducted at steady state conditions, with primary interest in the mean value of each measurand. The choice of sample frequency and sample size varied based on the purpose of the measurement. For setting the various combustor simulator flows, the sample frequency was set at 200 Hz with 400 points taken to get an average. This gave a sample time of 2 seconds, which provided reasonably quick feedback to the experimenter setting the flows. In measuring the vane pressure distribution, the sampling size was increased by a factor of 2, thereby increasing the sample time to 4 seconds. Inlet total pressure profile measurements were taken at 200 Hz with a sample size of 2000 points. Similar to the total pressure measurements, the sample frequency for thermal field measurements was 200 Hz and the sample size was 2000 points. The primary concern in the thermal field measurements was the sampling time. Measurements were taken for varying sample times from 5 seconds to 20 seconds to determine the impact on the resulting thermal field. A sampling time of 10 seconds was found to be sufficient to get a good average temperature. For recording endwall temperatures during infrared imaging, the sample frequency was 200 Hz and the sample size was 400 to give a data point every two seconds. From this temperature time history, the mean and standard deviation over the time of the test were determined and used in infrared camera calibration.

4.11 Measurement Uncertainties

Methods outlined by Moffat (1988) were used to describe the uncertainties in the experimental results. In estimating the uncertainty in measured and calculated quantities, both bias and precision errors were considered. These elemental errors were combined to give an overall uncertainty in a measured quantity using the root-sum-squares method. This method is expressed mathematically in Equation 4.14,

$$u_x = \pm\sqrt{e_{bias}^2 + e_{precision}^2} \tag{4.14}$$

where u_x represents the uncertainty in the measured quantity x. Estimates of the bias error were based on the transducer manufacturer's specifications of accuracy, while estimates of precision error were based on statistical analysis of the data assuming a 95% confidence interval. To estimate the precision uncertainty of a measurement, multiple readings were taken, typically on the order of 100, the sample standard deviation was calculated using Equation 4.15, and multiplied by the appropriate Student t factor.

$$S_x = \sqrt{\frac{1}{N-1}\sum_{i=1}^{N}\left(x_i - \bar{x}\right)^2} \tag{4.15}$$

In all instances, the value of t was taken to be 2, which corresponds to 60 independent measurements and a 95% confidence interval. Thus, the estimate of precision uncertainty can be expressed by Equation 4.16.

$$e_{precision} = \pm t_{60,95\%} S_x \tag{4.16}$$

The uncertainties in calculated quantities were estimated using the second power law of Kline and McClintock (1953). The second power law is derived from the linearized approximation of the Taylor series expansion for the calculated quantity and is odds-preserving. Mathematically, the uncertainty in a calculated quantity, $F = f(x_1,x_2,\ldots,x_n)$, due to the uncertainties in measured quantities, x_i ($i = 1,\ldots,n$), is expressed by Equation 4.17.

$$u_F = \pm\sqrt{\sum_{i=1}^{n}\left(\left.\frac{\partial F}{\partial x_i}\right|_{x=\bar{x}_i} u_{x_i}\right)^2} \tag{4.17}$$

Application of this method is largely straightforward, however, if applied blindly in certain situations, the second power law can yield conservatively high estimates of uncertainty. In particular, this situation arises when the calculated quantities are based on a difference in measured quantities. As an example, consider the uncertainty in a

calculated temperature difference, T_2 - T_1. If the bias and precision errors in both measurements are assumed to be independent of one another, the resulting uncertainty in the temperature difference may be overestimated. To illustrate this point, assume the measurement device for T_1 has a stated accuracy of ±1°C and a precision error of ±0.4°C, while that for T_2 has a stated accuracy of ±1.2°C and a precision error of ±0.5°C. Using these values, the individual uncertainties in T_1 and T_2 are ±1.1°C and ±1.3°C, respectively, and application of the second power law results in an uncertainty of ±1.7°C for the temperature difference. Now suppose the two measurement devices are brought into thermal equilibrium and observed to consistently differ in reading by approximately 0.3°C. This observed difference can be considered the bias error in the temperature difference. Using this observed error instead of the individual bias errors of the two devices, the calculated uncertainty in the temperature difference drops significantly to ±0.7°C. Furthermore, if the observed difference in the temperature readings is consistent in both sign and magnitude, it stands to reason that the bias error can be eliminated altogether through simple correction. To take the latter approach in estimating the uncertainty of a difference between measured values, it is essential that the experimenter observe the relative output of the measurement devices under identical conditions.

The two primary quantities of interest in this investigation are endwall adiabatic effectiveness, η, and non-dimensional flow temperature, θ, both of which are defined as the ratio of temperature differences. To make a fair assessment of the uncertainties in these calculated quantities, the methodology discussed above was employed. Though the two quantities are similar in definition, their associated uncertainties are not the same due to different means of measurement.

Endwall adiabatic effectiveness is defined in Equation 4.18, where T_{ms} is the measured midspan flow temperature, T_c is the measured coolant temperature, and T_{aw} is the measured adiabatic endwall temperature.

$$\eta = \frac{T_{ms} - T_{aw}}{T_{ms} - T_c} \tag{4.18}$$

While the midspan and coolant flow temperatures were measured using thermocouples, the adiabatic wall temperature was measured with the infrared camera. As previously mentioned, calibration of the camera was accomplished through comparison with multiple endwall mounted thermocouples. The uncertainty in the numerator is predominantly associated with this calibration process. From experience, the bias uncertainty in the numerator is estimated to be 1°C, while the precision uncertainty is estimated to be 0.4°C. Throughout this investigation, excellent agreement between thermocouples was observed. For the two thermocouple rakes, agreement between thermocouples was better than 0.1°C. Based on these observations, the bias uncertainty in the denominator is conservatively estimated at 0.3°C. From statistical analysis of the data, the precision uncertainty in the denominator is estimated to be 0.4°C. Using these estimates and assuming a nominal value for the denominator of 28°C, the calculated uncertainty in adiabatic effectiveness is $\delta\eta = \pm 0.04$ for nominal values between 0.4 and 0.8.

Non-dimensional flow temperature is defined in Equation 4.19, where T_{ms} and T_c are as defined above, and T is the measured flow temperature.

$$\theta = \frac{T_{ms} - T}{T_{ms} - T_c} \tag{4.19}$$

Unlike endwall adiabatic effectiveness, all temperatures associated with this quantity were measured using thermocouples. The bias and precision uncertainties for both numerator and denominator are estimated to be 0.5°C and 0.4°C, respectively. The resulting uncertainty in θ is $\delta\theta = \pm 0.03$.

Uncertainties in other measured and calculated quantities are summarized in Table 4.6. Maximum uncertainty in the vane pressure distribution, C_p, was primarily due to the uncertainty in cascade inlet dynamic pressure. Maximum uncertainty in the inlet nondimensional total pressure distributions, Δp_o, was calculated to be $\delta\Delta p_o = \pm 0.1$, also predominantly due to uncertainty in the inlet dynamic pressure. Flow velocities measured with the LDV (V_s and V_z) have relatively low uncertainty relative to flow velocity measured using a pitot-static probe (U). Uncertainty values for V_s and V_z were

assumed from a similar investigation by Kang and Thole (1999), who performed a rigorous analysis. The pitot-static probe was found to be adequate for measuring flow velocities above approximately 10 m/s. At lower velocities, the precision uncertainty becomes overwhelmingly large, giving poor overall uncertainty. The pitot-static probe used in this investigation was only used as a diagnostic tool. No measurement results for the probe are presented.

Table 4.1 Discharge coefficients used to calculate combustor simulator flow rates.

Combustor Simulator Feature	C_d	D_{hole} (cm)	N
Panel 1	0.74	0.76	202
Panel 2	0.73	0.76	478
Panel 3	0.73	0.76	413
Panel 4	0.74	0.76	130
Slot	0.70	0.99	13
Dilution 1	-	8.5	3
Dilution 2	-	12.1	2

Table 4.2 Typical operating parameters for the various windtunnel thermal conditioning elements.

Duct Heater	Power Output	Zone 1 (Upper)	100% (18.3 kW)
		Zone 2 (Middle)	100% (18.3 kW)
		Zone 3 (Lower)	100% (18.3 kW)
	Exit Air Temperature	Zone 1 (Upper)	86 °C
		Zone 2 (Middle)	82 °C
		Zone 3 (Lower)	87 °C
	Sheath-mounted Thermocouple		153 °C
Main Heat Exchanger	Water Supply		Tap
	Flow Rate		2-3 gpm
	Supply Temperature		~15 °C
Secondary Heat Exchangers	Water Supply		Chiller
	Flow Rate		10 gpm
	Supply Temperature		8-10 °C

Table 4.3 Summary of combustor simulator flow settings for the four tested conditions.

Percent of Exit Mass Flow (Momentum Flux Ratios)				
	Slotless Configuration		**Slotted Configuration**	
	$\Delta p_{o,max} \approx 1$	**$\Delta p_{o,max} \approx 2$**	**0.4% Slot Flow**	**0.8% Slot Flow**
Primary	42.8	44.4	42.0	42.7
Panel 1	1.2 (9)	0 (0)	1.2 (9)	1.2 (9)
Panel 2	3.5 (13)	0 (0)	3.5 (13)	3.5 (13)
Panel 3	4.6 (13)	7.4 (42)	4.6 (13)	4.6 (13)
Panel 4	2.1 (9)	2.6 (14)	2.1 (9)	2.1 (9)
Dilution 1	8.5 (129)	8.8 (143)	8.5 (129)	8.5 (129)
Dilution 2	8.7 (31)	9.0 (41)	8.7 (31)	8.7 (31)
Slot	-	-	0.42	0.84

Table 4.4 Experimental test matrix.

Test #	Cascade Configuration				Inlet Total Pressure Profile	
	Baseline	**Filleted**	**1X Slot Flow**	**2X Slot Flow**	$\Delta p_{o,max} \approx 1$	$\Delta p_{o,max} \approx 2$
1	✓		No backward-facing slot.		✓	
2		✓			✓	
3	✓					✓
4		✓				✓
5	✓		✓		✓	
6		✓	✓		✓	
7	✓			✓	✓	
8		✓		✓	✓	

Table 4.5 Pressure transducers utilized and their specifications.

Manufacturer	Model	Input Range	Output Range	Accuracy
Omega	PX653-0.5D5V	0-0.5 in. H_2O	1-5 Vdc	±0.25% FS
Omega	PX653-02D5V	0-2 in. H_2O	1-5 Vdc	±0.25% FS
Setra	2641-R25WD	0-0.25 in. H_2O	0-5 Vdc	±1% FS
Setra	2641-0R5WD	0-0.5 in. H_2O	0-5 Vdc	±0.25% FS
Setra	2641-0R5WD	0-0.5 in. H_2O	0-5 Vdc	±0.25% FS
Setra	2641-0R5WD	0-0.5 in. H_2O	0-5 Vdc	±0.25% FS
Setra	2641-005WD	0-5 in. H_2O	0-5 Vdc	±0.25% FS
Setra	2641-005WD	0-5 in. H_2O	0-5 Vdc	±0.25% FS

Table 4.6 Uncertainty estimates for measured and calculated quantities.

Value	Uncertainty Estimate
η	±0.04
θ	±0.03
C_p	±2.1
Δp_o	±0.1
V_s	±1% near vane-endwall
V_z	±1.5% near vane endwall
Tu	±3.2%
U (Pitot tube)	±0.7 m/s at 30 m/s

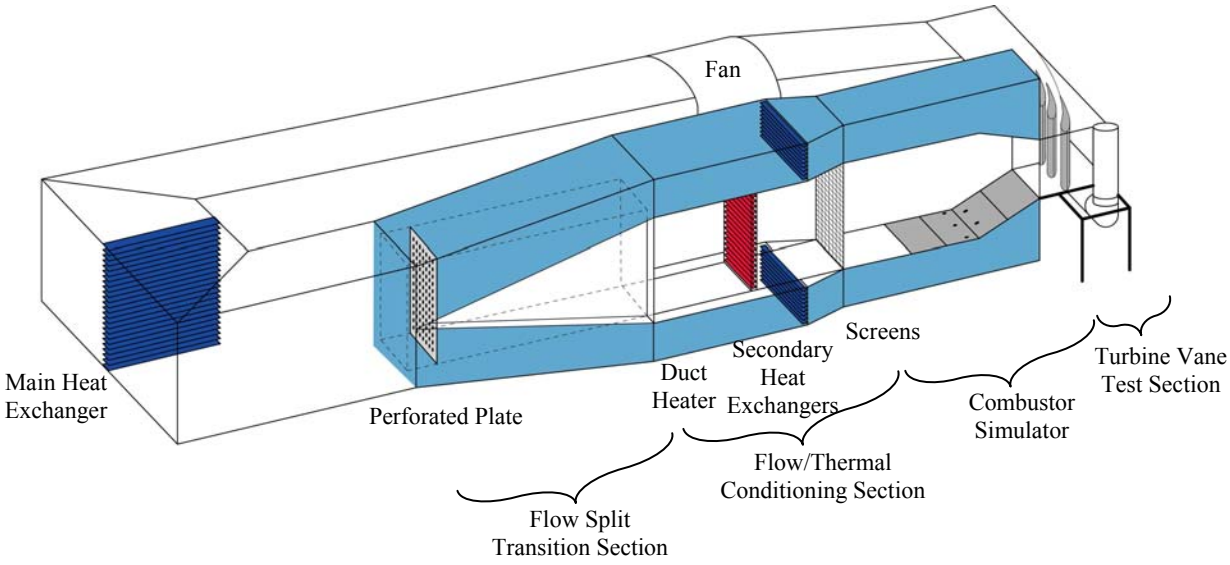

Figure 4.1 Combustor simulator, vane cascade wind tunnel (Barringer et al., 2002).

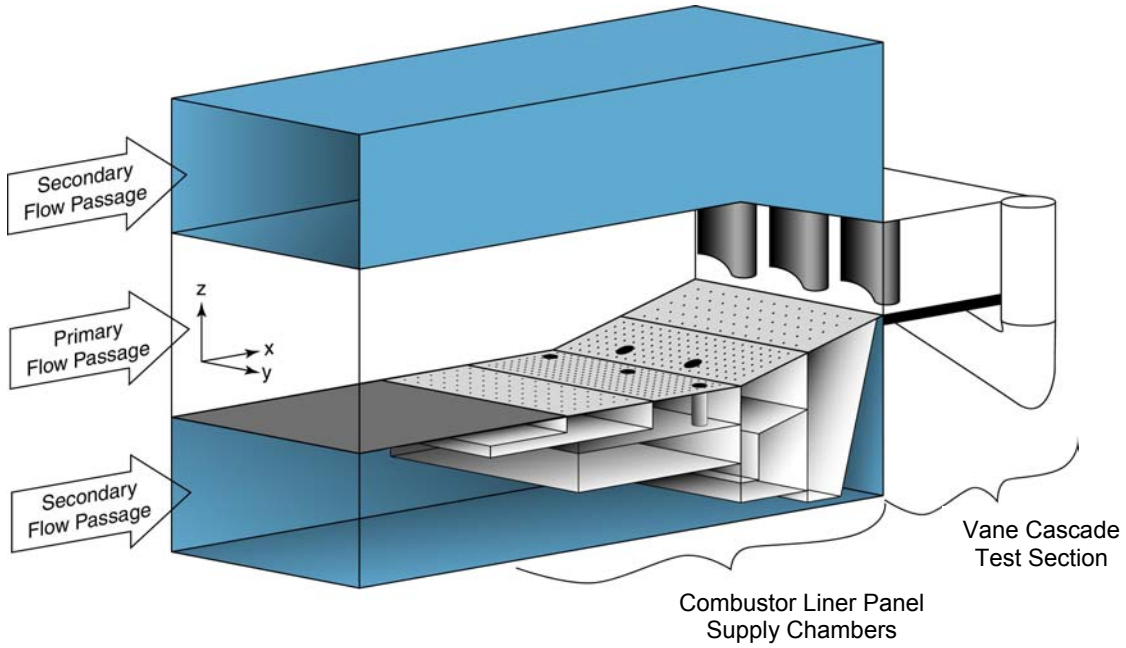

Figure 4.2 Schematic of the combustor simulator illustrating individual liner and dilution flow supply chambers (Barringer et al., 2002).

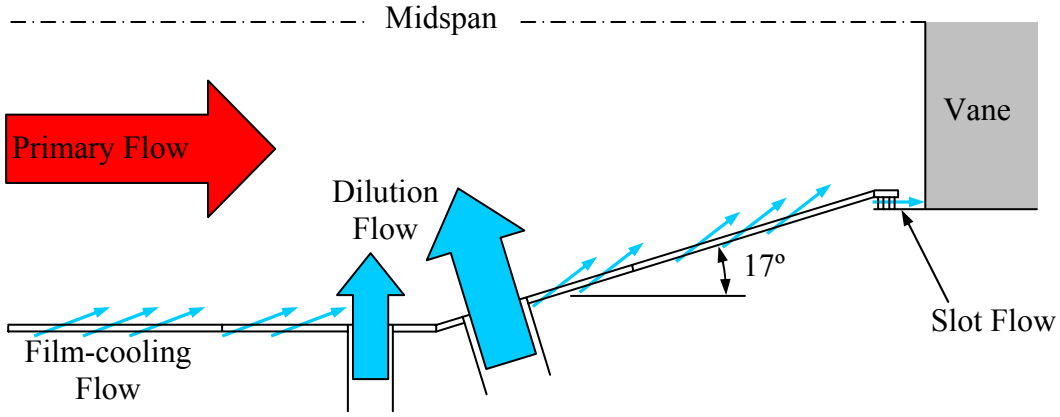

Figure 4.3 Schematic of the large-scale combustor simulator and turbine vane cascade.

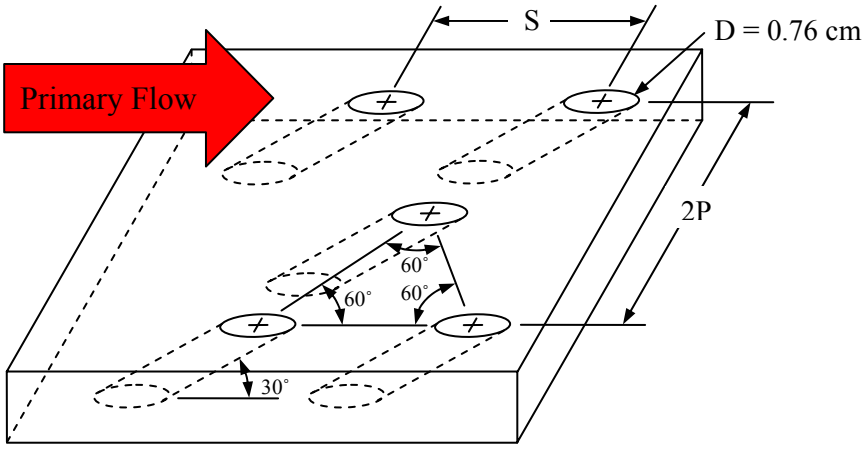

Liner Geometric Feature	P/D	S/D
Panel 1	5.0	5.8
Panel 2	3.0	3.5
Panel 3	3.0	3.5
Panel 4	7.1	7.1
Dilution Row 1	60($5.4D_1$)	-
Dilution Row 2	60($3.8D_2$)	-

Figure 4.4 Details of the film-cooling hole pattern for each of the combustor simulator liner panel (Barringer et al., 2002).

Figure 4.5 Photograph of the 55kW duct heater bank used to elevate the primary flow temperature.

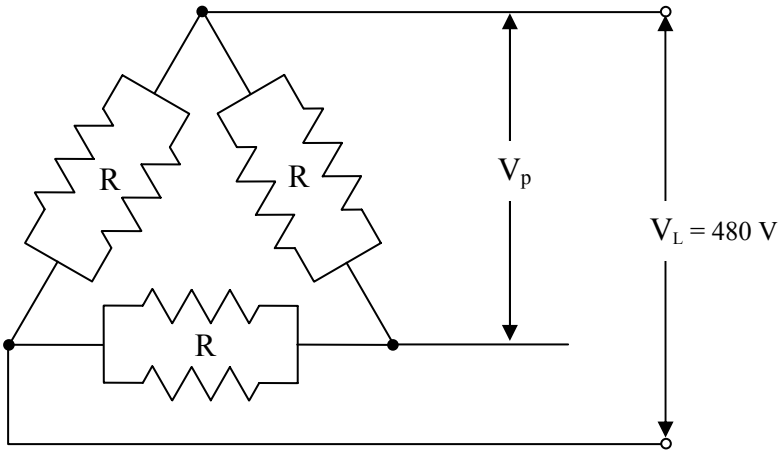

Figure 4.6 3-Phase Delta electrical wiring configuration for each of the heater zones.

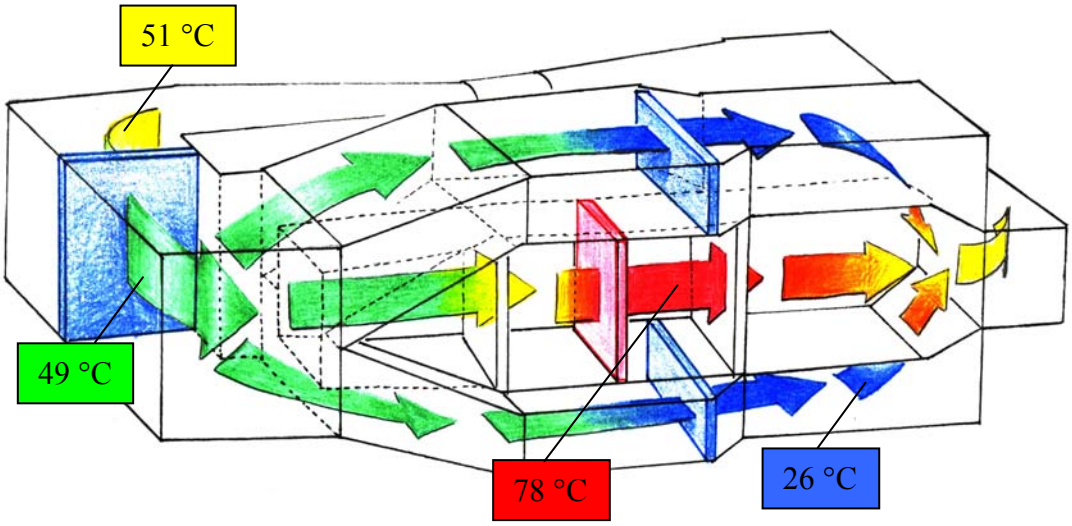

Figure 4.7 Illustration of the wind tunnel thermal conditioning system with typical operating temperatures.

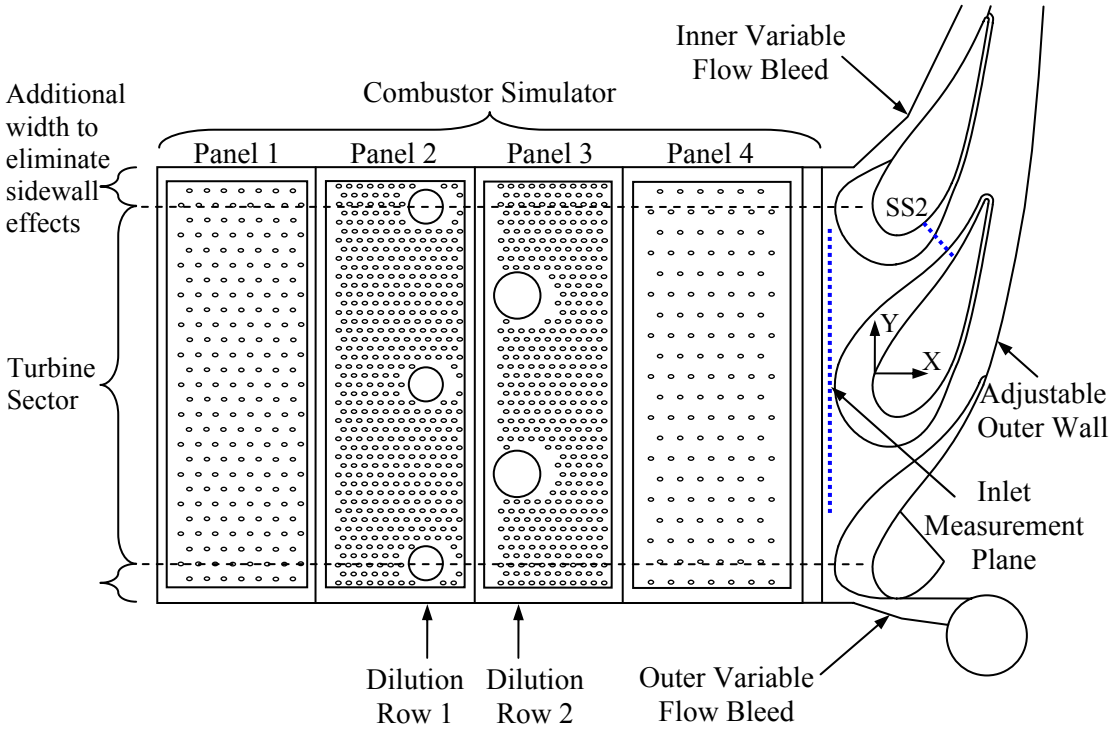

Figure 4.8 Schematic of the combustor simulator and turbine vane cascade.

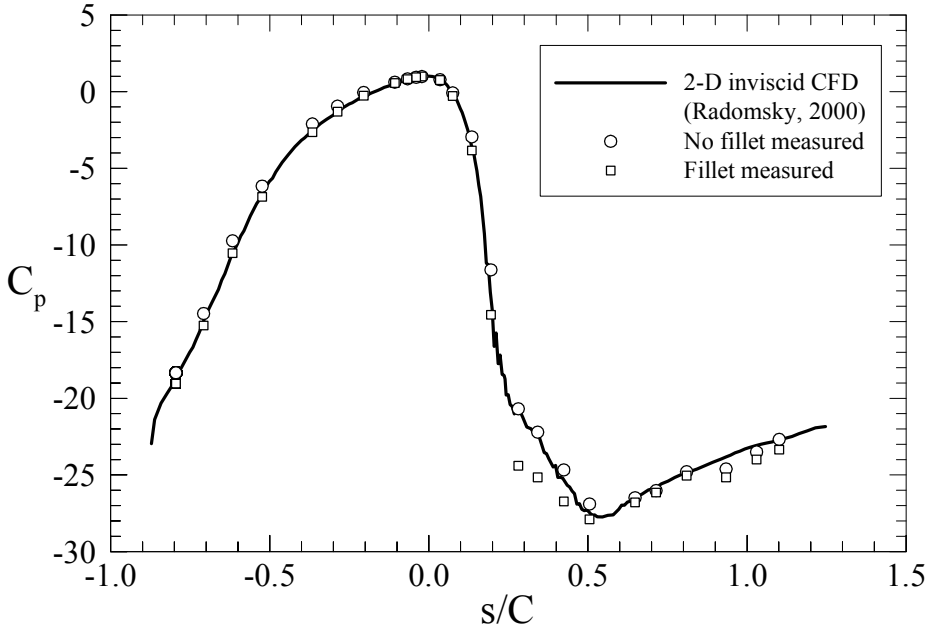

Figure 4.9 Comparison of measured pressure coefficient distributions with and without the fillet to a 2-D inviscid prediction.

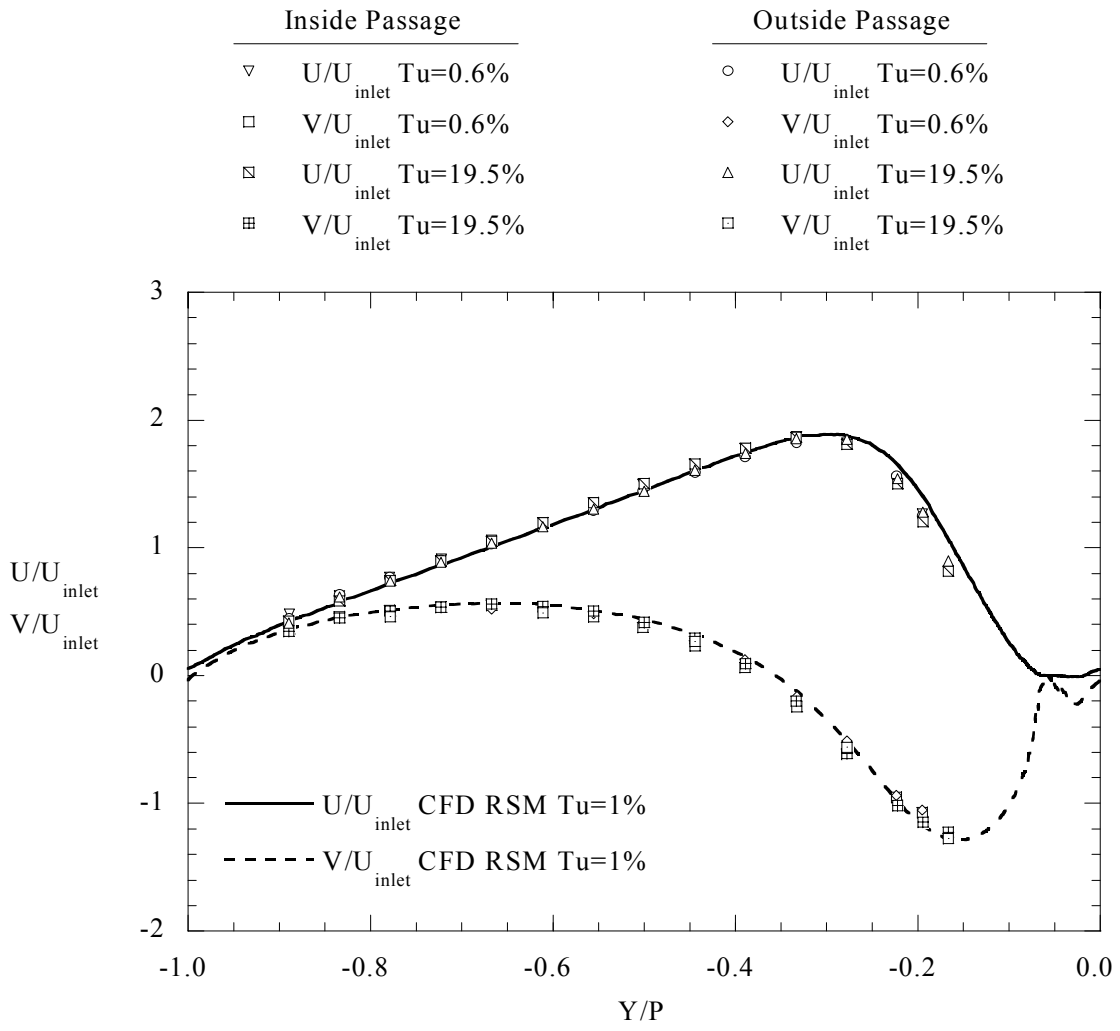

Figure 4.10 Normalized streamwise and pitchwise velocities along a line connecting geometric stagnation points, indicating passage flow periodicity (Radomsky, 2000).

Figure 4.11 Photograph of the windtunnel vane cascade.

Figure 4.12 Photographs of the fillet installation and bleed transitions.

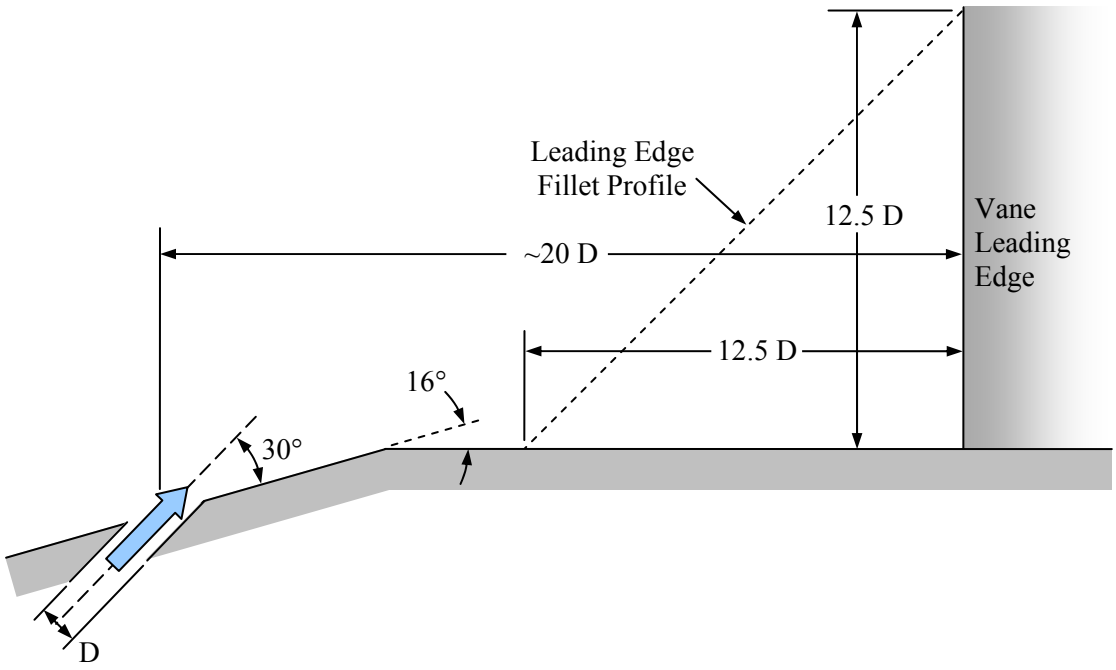

Figure 4.13 Baseline unfilleted, slotless combustor simulator configuration.

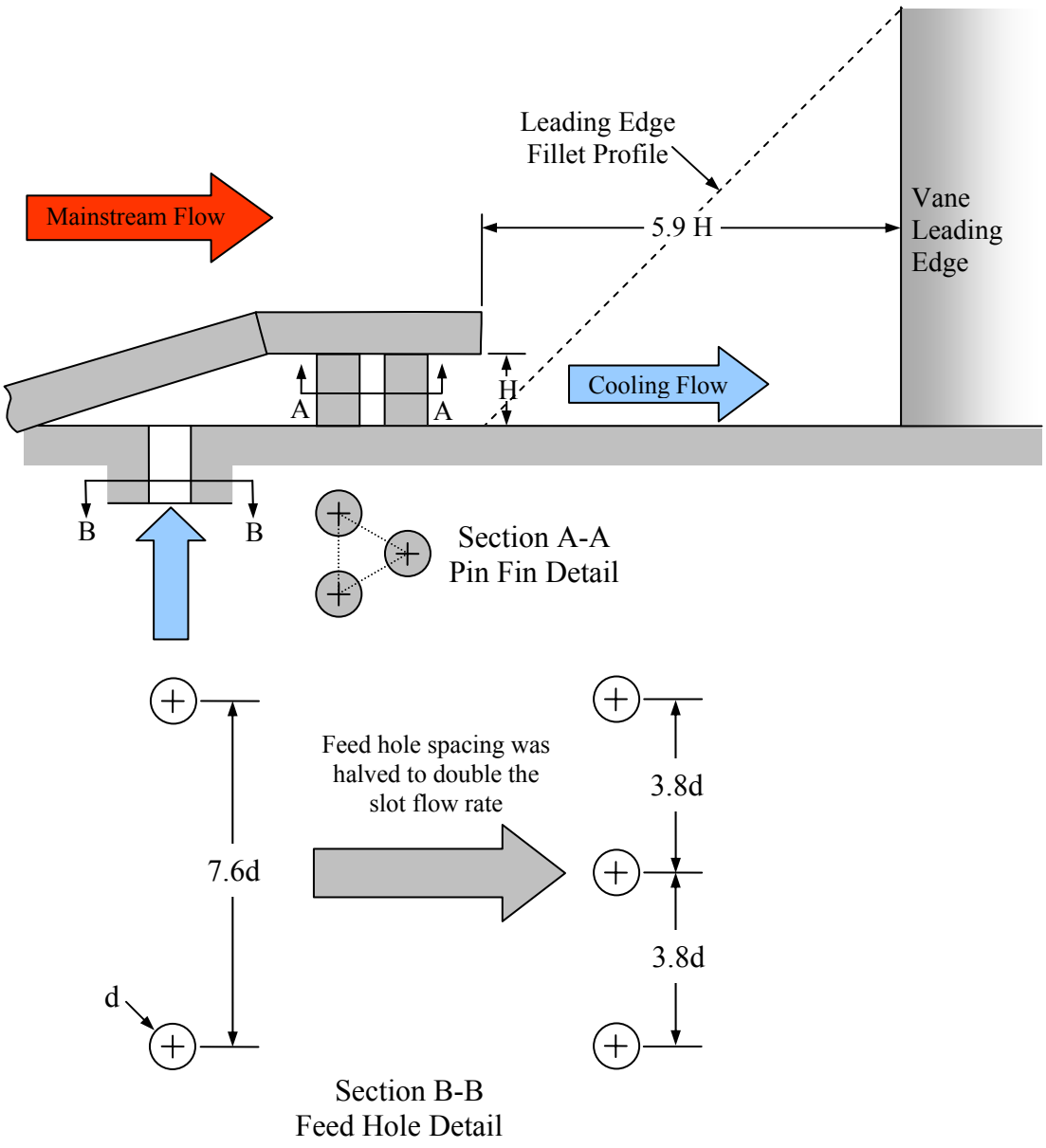

Figure 4.14 Modified combustor/cascade interface to accommodate testing of the linear fillet with a backward-facing slot.

(a)

(b)

Figure 4.15 Photographs of the modified slot installation looking **(a)** upstream at the slot opening, and **(b)** downstream at the modified combustor/cascade interface.

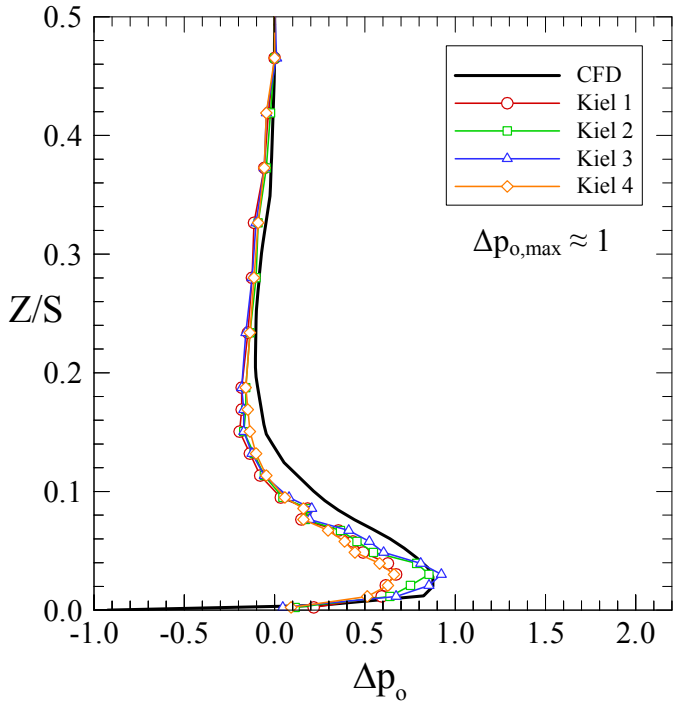

(a)

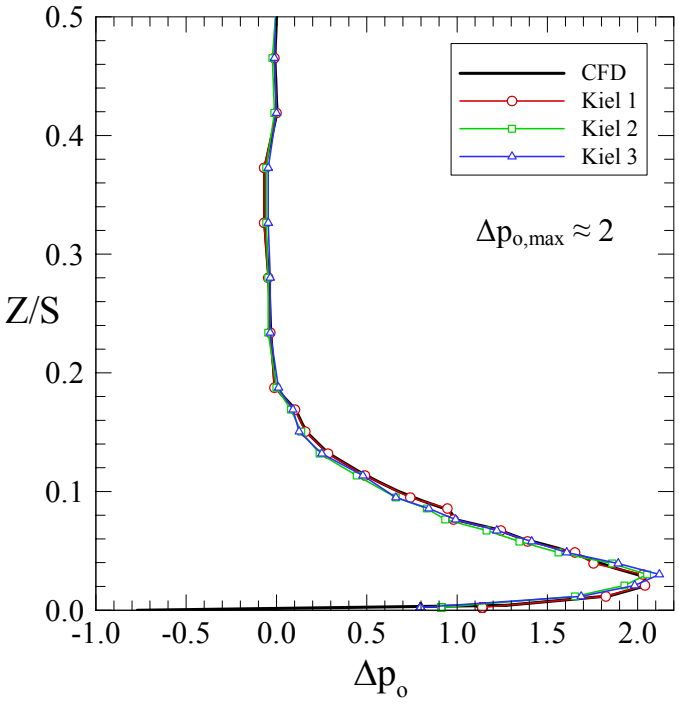

(b)

Figure 4.16 The **(a)** design and **(b)** off-design cascade inlet total pressure profiles investigated.

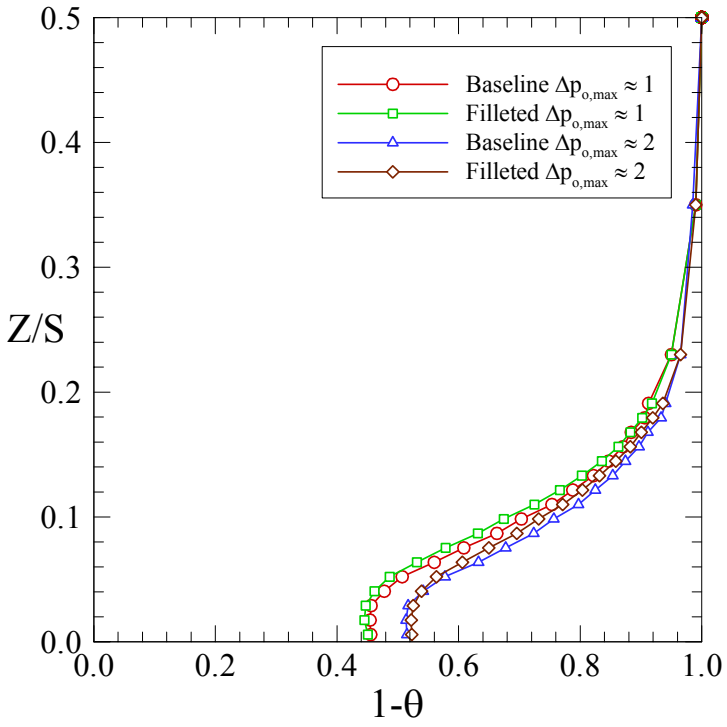

Figure 4.17 Comparison of the resultant inlet nondimensional temperature profiles for the two inlet total pressure profiles considered.

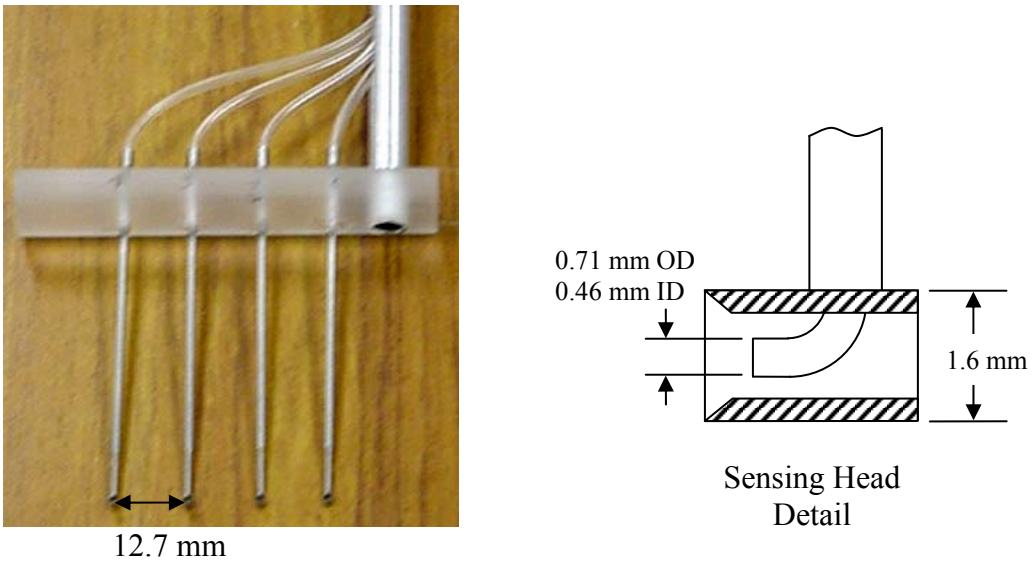

Figure 4.18 Photograph of the Kiel probe rake utilized in measurement of the cascade inlet total pressure profile.

Figure 4.19 Typical 30 AWG Type E welded thermocouple junction used to measure surface and flow temperatures throughout the windtunnel.

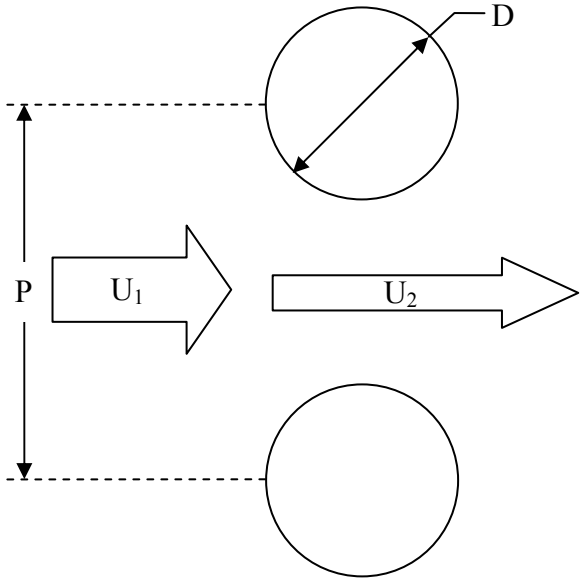

P/D	Blockage	U_2/U_1
2	50%	2.00
3	33%	1.50
4	**25%**	**1.33**
5	20%	1.25
6	17%	1.20

Figure 4.20 Influence of thermocouple rake element spacing on the flowfield.

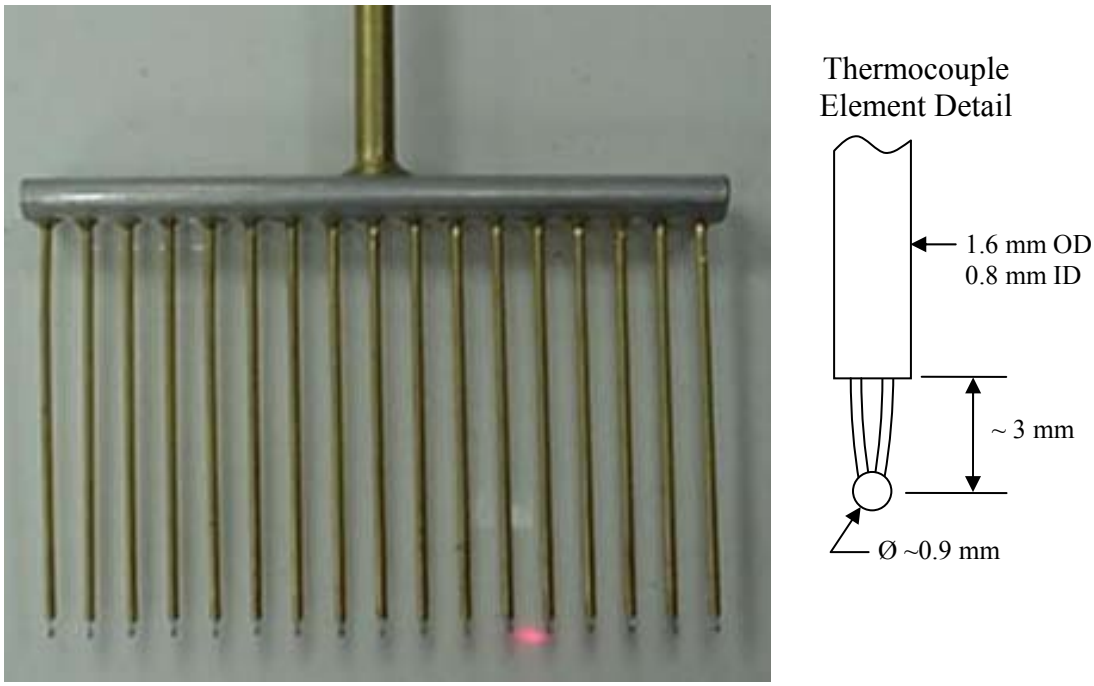

Figure 4.21 Photograph of linear thermocouple rake designed for baseline testing.

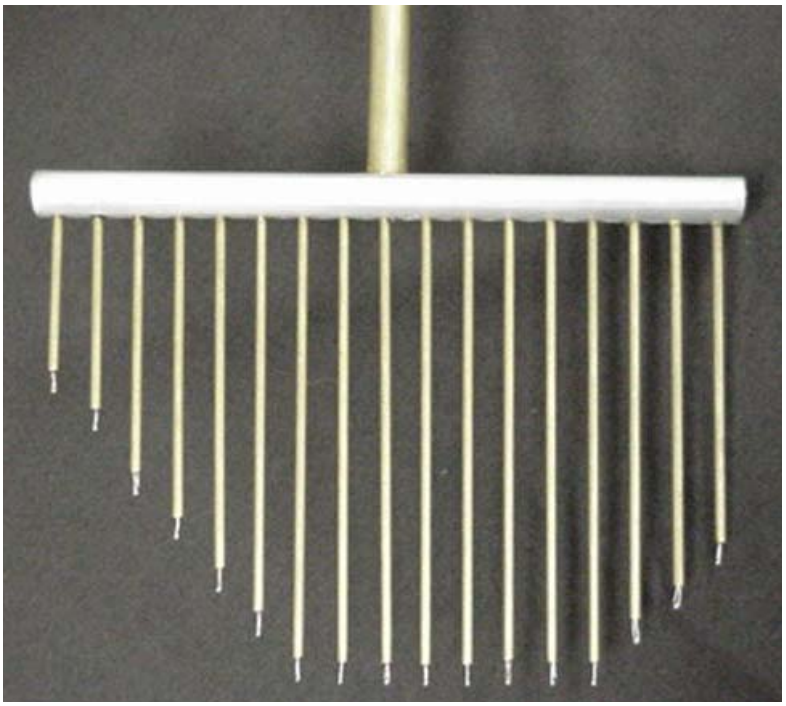

Figure 4.22 Photograph of profiled thermocouple rake designed for fillet testing.

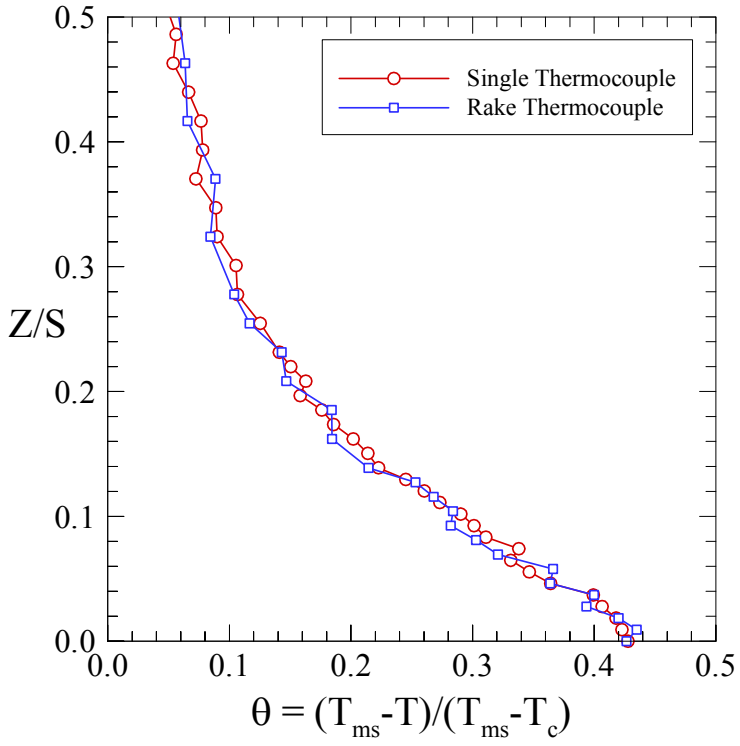

Figure 4.23 Comparison of temperature traverse results between a rake thermocouple and a single element thermocouple performed in the SS2 measurement plane.

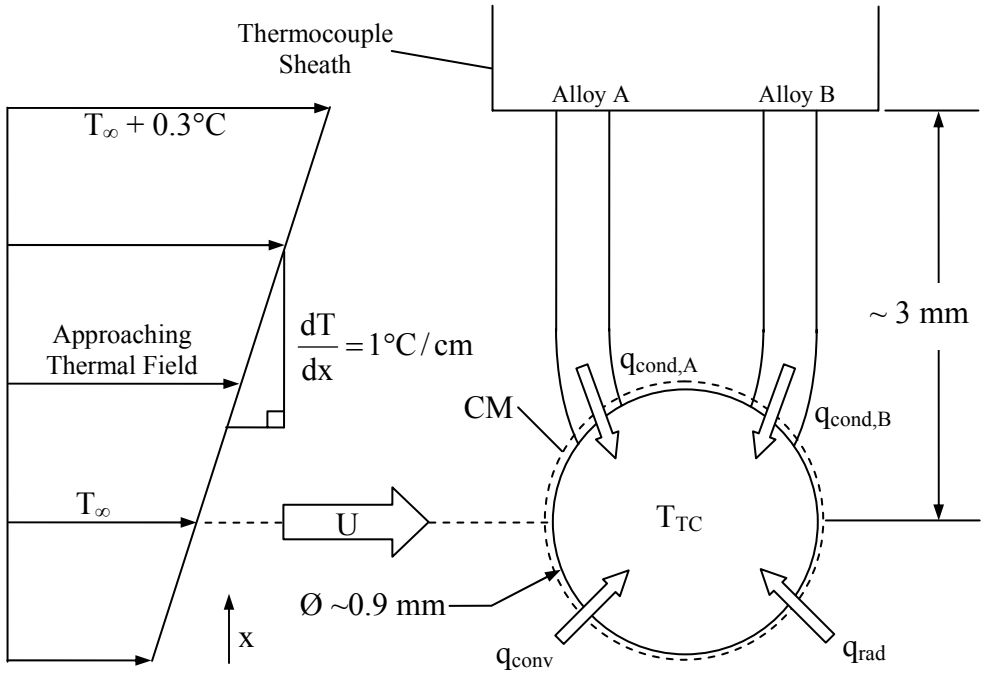

Figure 4.24 Schematic of the thermocouple junction modeling approach used in estimating measurement error due to conduction and radiation.

Figure 4.25 Photograph of the Inframetrics Model 760 infrared camera and controller used for thermal mapping of the vane passage endwall.

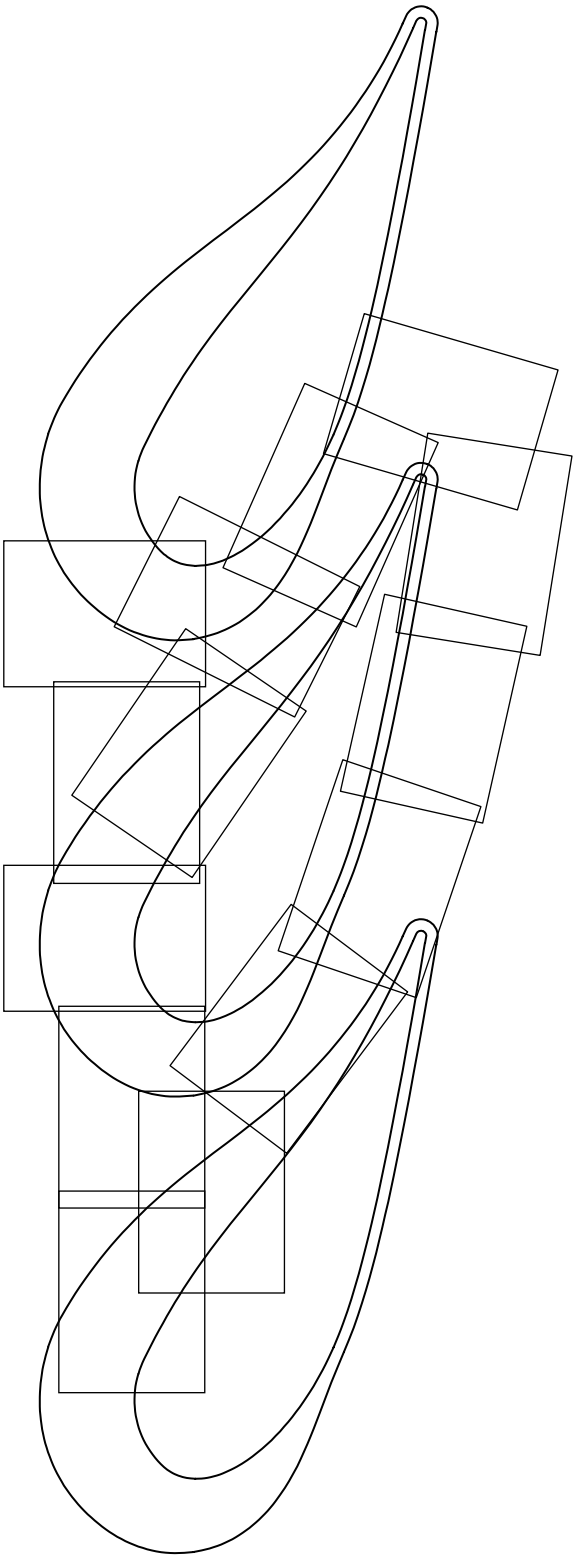

Figure 4.26 IR camera imaging locations.

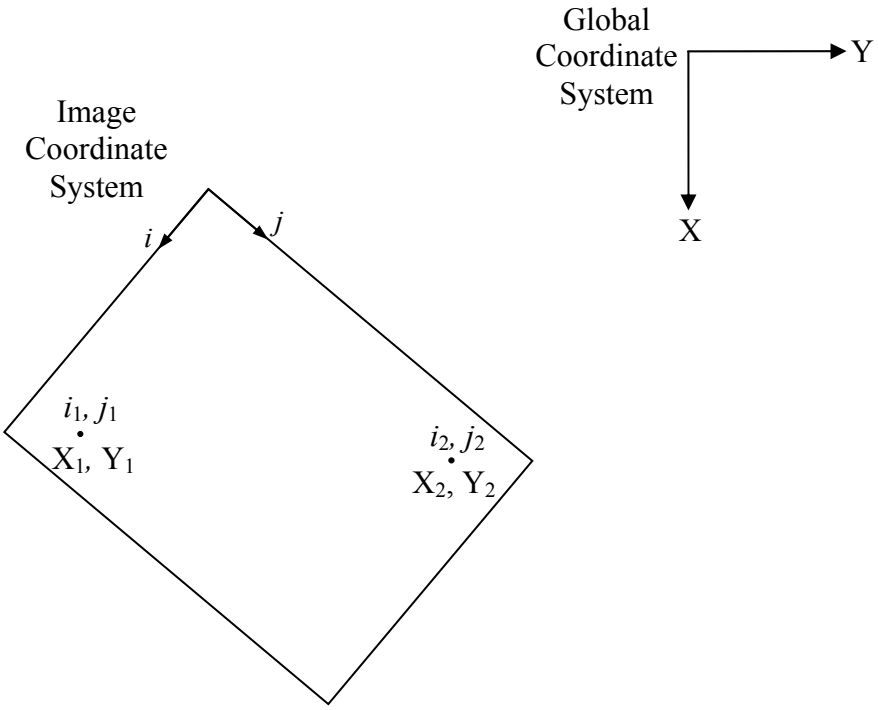

Figure 4.27 Schematic illustrating infrared image orientation determination.

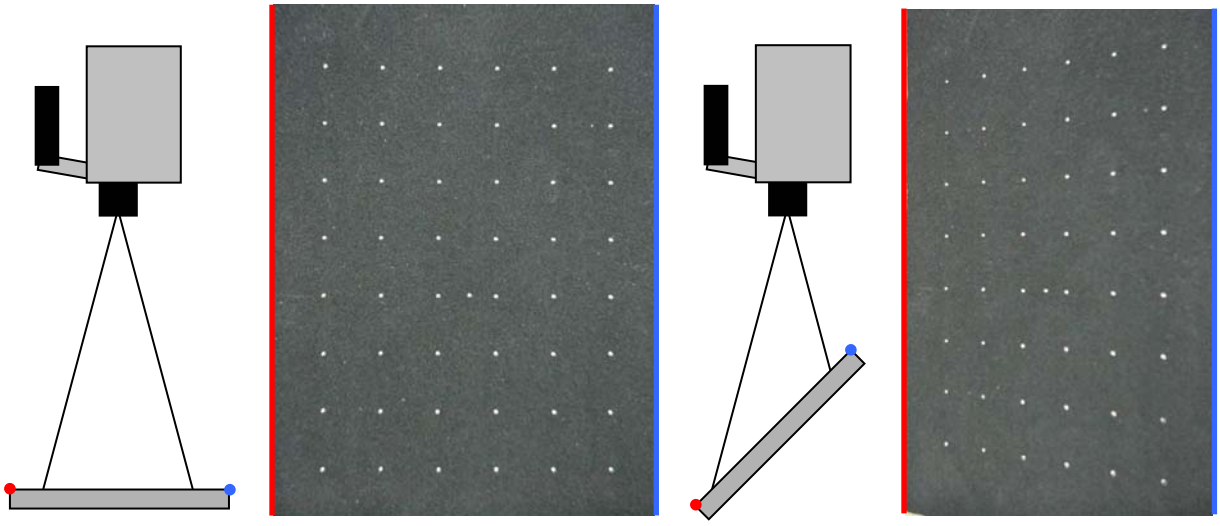

Figure 4.28 Illustration of image distortion that occurs when imaging a non-planar surface.

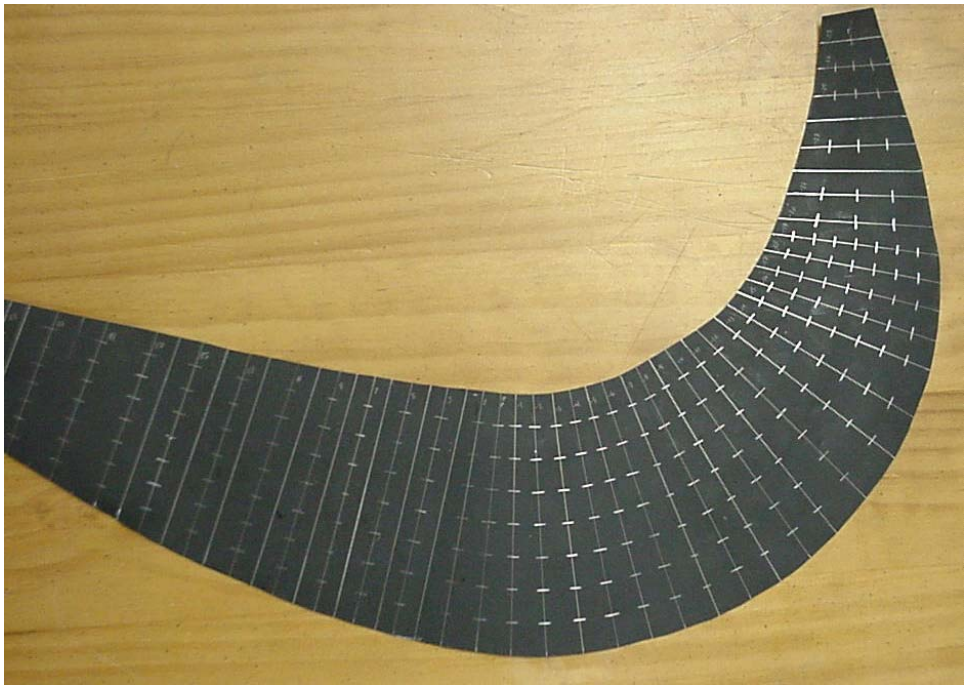

Figure 4.29 Photograph of the fillet template used for fillet distortion correction.

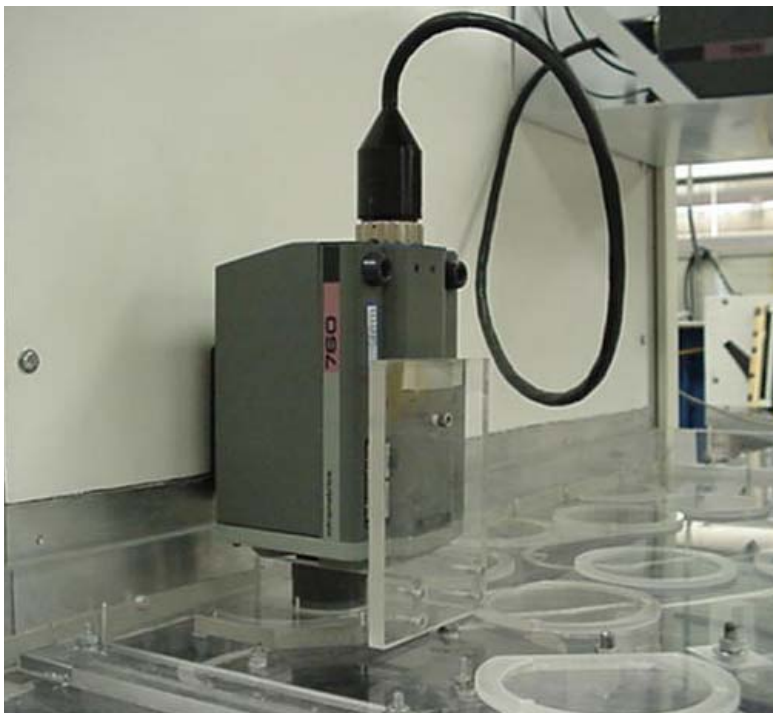

Figure 4.30 Photograph of the infrared camera and acrylic mounting fixture used for camera alignment.

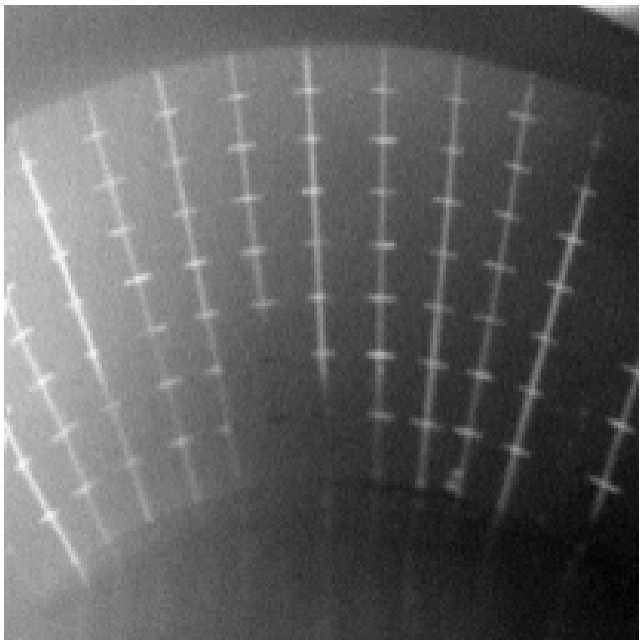

Figure 4.31 Typical calibration image of the fillet template taken for fillet distortion correction.